Thermodynamic Contribution to Vortex Alignment and Rapid Intensification of Hurricane Sally (2020)

ŽELJKA STONE,[a] G. R. ALVEY III,[b,c] J. P. DUNION,[b,c] M. S. FISCHER,[b,c] D. J. RAYMOND,[a] R. F. ROGERS,[b] S. SENTIĆ,[a] AND J. ZAWISLAK[b,c]

[a] *Climate and Water Consortium and Physics Department, New Mexico Institute of Mining and Technology, Socorro, New Mexico*
[b] *NOAA/OAR/AOML/Hurricane Research Division, Miami, Florida*
[c] *Cooperative Institute for Marine and Atmospheric Studies, University of Miami, Miami, Florida*

(Manuscript received 24 July 2022, in final form 18 January 2023)

ABSTRACT: As a part of the Tropical Cyclone Rapid Intensification Project (TCRI), observations were made of the rapid intensification of Hurricane Sally (2020) as it passed over the Gulf of Mexico. High-altitude dropsondes and radar observations from NOAA's Gulfstream IV, radar observations from WP-3D aircraft, the WSR-88D ground radar network, satellite images, and satellite-detected lightning strikes are used to apply recently developed theoretical knowledge about tropical cyclone intensification. As observed in many other tropical cyclones, strong, bottom-heavy vertical mass flux profiles are correlated with low (but positive) values of low- to midlevel moist convective instability along with high column relative humidity. Such mass flux profiles produce rapid spinup at low levels and the environmental conditions giving rise to them are associated with an intense midlevel vortex. This low-level spinup underneath the midlevel vortex results in the vertical alignment of the vortex column, which is a key step in the rapid intensification process. In the case of Sally, the spinup of the low-level vortex resulted from vorticity stretching, while the spinup of the midlevel vortex at 6 km resulted from vorticity tilting produced by the interaction of convective ascent with moderate vertical shear.

SIGNIFICANCE STATEMENT: The purpose of this study is to investigate the rapid intensification of Hurricane Sally as it was approaching the Florida Panhandle. We do that by analyzing an unprecedented dataset from the NOAA WP-3D and Gulfstream-IV aircraft, together with ground-based radar and satellite data. We find that both the dynamics (vorticity structure and evolution) and thermodynamics (instability index, saturation fraction, heating/mass flux profiles) need to be considered in diagnosing intensification processes. Further field projects with continuous high-altitude dropsondes and research are needed to see if these are applicable to other reformation events as well as genesis.

KEYWORDS: Convection; Hurricanes/typhoons; Potential vorticity

1. Introduction

Forecasting the intensification of tropical cyclones (TCs), especially rapid intensification (RI), is a difficult problem and progress has been slow (Cangialosi et al. 2020). Though TC intensification is often measured in terms of maximum winds or minimum surface pressures, the variable most closely related to the physical process of intensification is the absolute vorticity. Nondivergent horizontal motions can move air parcels around, but they cannot change the magnitude of parcel vorticity. For this reason, convection, with its vertical motions and associated horizontal divergence, plays a key role in cyclone intensification. Two factors are important for cyclone intensification: how the environment controls the location, strength, and form of convection and how convection affects the absolute vorticity.

Wind shear is often cited as a factor in suppressing cyclone intensification (e.g., DeMaria et al. 2005; Rios-Berrios and Torn 2017). With shear, low and midlevel vortices are often misaligned, with intensification thought to occur when these vortices come into vertical alignment by some process. Rios-Berrios et al. (2018) present a review of attempts to understand TC intensification in shear as well as similar hypotheses for how this works. In particular, on the basis of ensembles of numerical simulations, they conclude that vortex alignment occurs as the result of reformation of the low-level vortex underneath the existing midlevel vortex via vertical stretching and possibly tilting induced at low levels. They infer that horizontal advection of the vortices is less important in this process.

Our recent observational work on tropical convection, much of it involving TCs, employs grids of dropsondes deployed from high altitude. Thermodynamic and wind fields are analyzed with roughly 100-km resolution (Raymond and López Carrillo 2011; López Carrillo and Raymond 2011; Raymond et al. 2011; Gjorgjievska and Raymond 2014; Juračić and Raymond 2016; Fuchs-Stone et al. 2020; Raymond and Fuchs-Stone 2021a). These observations cannot resolve convective cells individually. However, they show the collective effects of convection important to TC dynamics and reveal emergent patterns of behavior pertinent to intensification that are not obvious from convective-scale observations or models. We use this technique to study the formation of Hurricane Sally (2020), which underwent a sudden vortex alignment near the start of a period of RI. These observations lend support to the hypothesis

Denotes content that is immediately available upon publication as open access.

Corresponding author: Željka Stone, zeljka.fuchs@nmt.edu

DOI: 10.1175/MWR-D-22-0201.1

of Rios-Berrios et al. (2018) and show more fully how this occurred in Sally.

The most important characteristics of mesoscale convective evolution on the 100-km scale inferred from the above work are the vertical mass fluxes, assumed to be largely associated with convection. These patterns are found not to be random, but are related to certain characteristics of the thermodynamic environment.

Of particular importance are the column relative humidity or saturation fraction (Sherwood 1999; Bretherton et al. 2004; Raymond et al. 2007; Neelin et al. 2009; Raymond and Fuchs-Stone 2021a) and the so-called instability index (Raymond et al. 2011). Saturation fraction is defined as

$$\mathrm{SF} = \int \rho r dz \Big/ \int \rho r^* dz, \tag{1}$$

where ρ is the density, r is the water vapor mixing ratio, r^* is the saturated mixing ratio, and the integral is over the depth of the troposphere. The instability index, a measure of the low to midtropospheric moist convective instability, is defined as

$$\mathrm{II} = s^*_{\mathrm{lo}} - s^*_{\mathrm{hi}}, \tag{2}$$

where s^*_{lo} and s^*_{hi} are, respectively, the 1–3- and 5–7-km means of specific saturated moist entropy, where the entropy definition is that of Emanuel (1994). Increased humidity is associated with stronger vertical mass fluxes. Counterintuitively, lower (but still positive) convective instability is also a predictor for stronger fluxes that in addition are more bottom-heavy (Raymond et al. 2014; Sessions et al. 2015; Sentić et al. 2015; Raymond and Flores 2016; Raymond and Kilroy 2019; Raymond and Fuchs-Stone 2021a), i.e., with mass flux peaking at lower elevations.

Convective instability, as defined in this case, must be distinguished from conditional instability, which measures the buoyancy of boundary layer parcels against the free tropospheric temperature profile. As defined in the above-cited work, the instability index compares the saturated moist entropy of the lower troposphere just above the boundary layer to that of the middle troposphere. This parameter thus depends solely on the temperatures of these two levels and excludes boundary layer processes. The counterintuitive fact that a more bottom heavy mass flux is associated with a lower instability index was shown by Raymond and Sessions (2007) in weak temperature gradient simulations, and confirmed in a number of numerical and field data studies cited above.

Boundary layer effects are encompassed in the third variable, deep convective inhibition:

$$\mathrm{DCIN} = s^*_{\mathrm{th}} - s_{\mathrm{bl}}, \tag{3}$$

where s_{bl} is the 0–1-km average of moist entropy and s^*_{th} is the 1.2–1.5-km average of the saturated moist entropy.[1] DCIN is an approximate measure of the maximum buoyancy deficit encountered by parcels ascending from the 0–1-km layer where positive values indicate greater convective inhibition. This deep layer was used by Raymond et al. (2003) in the original definition of DCIN since it was more representative of the layer tapped by deep convection compared to more traditional definitions of convective inhibition.

Two more variables that are important to tropical cyclogenesis and intensification are the surface moist entropy flux and the sea surface temperature (SST). Algorithms for calculating surface fluxes are well established and are not repeated here (Raymond 1995; Maloney and Esbensen 2003; Maloney and Sobel 2004; Raymond et al. 2006, and others). The SST makes a strong contribution to the moist entropy flux but is only one factor; the boundary layer wind and moist entropy affect the flux as well. The moist entropy flux specifies the amount of entropy added to the atmosphere, whereas the SST to a large extent controls parcel buoyancy.

As shown by Singh and O'Gorman (2013), smaller buoyancies require moister environments for convection to survive the entrainment of environmental air [see also James and Markowski (2010)]. If it is too dry, convection fails, but moistens the environment, thus making conditions more favorable for subsequent convection. If the environment is too moist, the convection produces excess precipitation, which then leads to drying of the column (Raymond et al. 2009; Raymond and Fuchs-Stone 2021a). The result is evolution of the environment toward an optimal value of column moisture, which is greater for smaller parcel buoyancy. For dry environments with weak convection, the moistening of the environment is weak and the optimum moisture may not be reached in a reasonable period of time. However, moisture evolution toward equilibrium is more rapid in strongly convective environments (Raymond 2000), which means that strongly convective environments rarely exhibit saturation fractions exceeding the equilibrium value. This "moisture quasi-equilibrium" process therefore sets a limit on the ability of convection to moisten the environment. This limiting moisture is an inverse function of the instability index—low values of the instability index result in higher equilibrium values of saturation fraction and vice versa.

Modeling provides useful insights into the thermodynamic control of convection. Raymond and Sessions (2007) and Sessions et al. (2015) explored the effect of variations in column moisture and low- to midtropospheric convective instability in weak temperature gradient simulations of convection (Raymond and Zeng 2005; Herman and Raymond 2014; Daleu et al. 2016; Raymond and Fuchs-Stone 2021b). Decreasing instability index and increasing saturation fraction both lead to increases in modeled precipitation rate. In addition, the decrease in instability index leads to more bottom-heavy convective mass flux profiles, i.e., with maximum mass flux in the lower troposphere, whereas the increase in humidity by itself does not (moisture quasi-equilibrium is suppressed in these simulations by independently specifying ambient temperature and humidity profiles).

Raymond and Kilroy (2019) analyzed the effect of saturation fraction, instability index, as well as deep convective inhibition on precipitation and lower tropospheric vertical mass

[1] Different versions of DCIN define slightly different altitude ranges for s^*_{th}.

flux in three different simulations of tropical cyclogenesis (the SST dependence was not studied because the same SST was used for all simulations). The three simulations were described in three different papers. All simulations were set in a large unsheared domain with a stretched grid and were initiated using the same initial weak vortex. Kilroy et al. (2017a) used warm rain cloud physics while Kilroy et al. (2018) employed full ice cloud physics. The third, Kilroy et al. (2017b) was a warm rain simulation in which boundary layer friction was turned off, resulting in spin up of a cyclone with rather odd structure. For each simulation, two time series were analyzed, an average over an inner core circular region 50 km in radius, centered in the computational domain, and an encompassing outer ring with radius range $50 < r < 100$ km. The inner core contained any eyewall that developed for the full period of all cases. The outer ring encompassed much of the outer rainband convection.

The six time series from the three simulations, taken jointly, provide a broad spectrum of convection against which to test the hypothesis that the variables discussed above, and in particular saturation fraction and instability index, are sufficient to predict the characteristics of convection in all stages and regions of TC. Surprisingly, these variables captured a large part of the variance in the 3–5-km layer-averaged vertical mass flux of convection, including that in the eyewall, early stage convection, and convection occurring in the outer rainbands.

The potential vorticity q connects the convective environment with the vorticity dynamics of the surrounding atmosphere. It may be approximated as

$$q = \frac{\Gamma \zeta_z}{\rho} \tag{4}$$

in most tropical environments, where ρ is the density, $\Gamma = \partial\theta/\partial z$ is the vertical potential temperature gradient, and ζ_z is the vertical component of absolute vorticity. In a balanced state, larger q is distributed between larger Γ and larger ζ_z, with greater weighting of Γ for potential vorticity anomalies with larger horizontal dimensions. Larger Γ in the low to midtroposphere corresponds to smaller instability index and smaller parcel buoyancies at middle and upper levels relative to low-level values, resulting in more bottom-heavy convection.

The instability index is a key predictor of strong upward mass flux in the inner core of all simulations, with a very nonlinear response. The strongest mass fluxes occur for $\mathrm{II} < 12\ \mathrm{J\ K^{-1}\ kg^{-1}}$. Instability index lower than this threshold also correlates with the onset of strong surface moist entropy fluxes, a good indicator of the spin up of the low-level cyclone. Since the instability index is a function of the strength of the cyclone vortex via the thermal wind equation, this is to be expected. In the outer ring, the saturation fraction is a somewhat stronger predictor of mass flux than the instability index, though the latter variable is still important.

The following picture emerges from the above results (Raymond et al. 2015). In a dynamically balanced environment the balanced temperature structure of the atmosphere is defined by the pattern of potential vorticity (Hoskins et al. 1985; Haynes and McIntyre 1987, 1990; Raymond 1992, 2012). Thus, via its effect on the temperature structure, the potential vorticity controls the instability index, which in turn sets an upper bound on the saturation fraction. The combination of these two parameters controls the statistical characteristics of convection in this picture.

Convection in turn modifies the vorticity structure via the advective, stretching, and tilting processes produced by the horizontal winds and the convective mass fluxes. These processes are encompassed in the flux form of the vorticity tendency equation (Haynes and McIntyre 1987; Raymond 1992; Raymond et al. 2014):

$$\frac{\partial \zeta_z}{\partial t} = -\nabla_h \cdot \mathbf{Z}, \tag{5}$$

where ∇_h is the horizontal gradient, and

$$\mathbf{Z} = \mathbf{v}_h \zeta_z - \boldsymbol{\zeta}_h v_z + \mathbf{k} \times (\mathbf{F} - \alpha' \nabla_h p) \tag{6}$$

is the horizontal flux of vertical absolute vorticity. In this equation $(\mathbf{v}_h, v_z)$ is the wind velocity, $\boldsymbol{\zeta}_h$ is the horizontal component of absolute vorticity, $\mathbf{F}$ is the horizontal component of friction, such as might occur due to eddy momentum fluxes in the boundary layer, α' is the deviation from the vertical profile of horizontally averaged specific volume, and p is the pressure. We ignore the frictional term since we do not consider frictional convergence in the boundary layer directly but assume that the low-level lifting due to frictional convergence is encapsulated in its effect on the deep convective inhibition. In addition, since the last term is several orders of magnitude smaller than the competing terms in our case, we ignore it also.

The first term in (6) expresses the horizontal flux of vertical vorticity and leads to a combination of stretching and horizontal advection in (5). The second term is the horizontal convergence of the vertical advection of horizontal vorticity. Physically, this represents the tilting of horizontal vorticity into the vertical but differs from the Lagrangian tilting term in the advective form of the vorticity equation. The Lagrangian form represents the tilting tendency in a vertically moving parcel whereas the Eulerian form shown here represents the tendency due to tilting at a fixed level.

Note that $\mathbf{Z}$ has no vertical component, meaning that there is no vertical flux of vertical absolute vorticity. The vorticity tendency in (5) depends on the reference frame due to the horizontal advection of vertical vorticity. In the present work we choose the reference frame co-moving with the TC. Note that the vorticity tendency in (5) is not a parcel derivative. Instead, it is the time derivative at a fixed point in the co-moving reference frame.

While much of the theoretical work examining the relationships among column moisture, low to midtropospheric convective instability, midlevel vorticity, mass flux profiles, and low-level vortex spinup described above was developed for genesis events, these concepts have recently been applied to vortex reformation events as well. Reformation typically involves mid and low-level vortex centers displaced significant distances from each other (e.g., 100 km or more), where the

low-level vortex redevelops underneath the existing midlevel vortex. Reformation has been observed to occur downshear of the low-level center in the presence of deep convection and widespread precipitation (Molinari et al. 2004, 2006; Molinari and Vollaro 2010; Nguyen and Molinari 2015; Chen et al. 2018). In an analysis of the intensification of Hurricane Hermine (2016), Rogers et al. (2020) noted that there was a substantial displacement of the midlevel center of Hermine downshear of the low-level center in the presence of persistent moderate shear. Repeated cycles of deep convection occurred downshear of the low-level center, which served to episodically moisten the downshear environment and intensify the midlevel center. After several such cycles of convective development and moistening, the thermodynamic environment downshear was characterized by a region of low instability index and high column moisture. A subsequent burst of deep convection resulted in the repositioning of Hermine's low-level center underneath the well-developed midlevel center. This region also contained a large amount of convection of moderate depth. Associated with this widespread deep and moderate convection was a bottom-heavy mass flux profile and pronounced vorticity stretching in the lower troposphere in a mesoscale domain surrounding the midlevel vortex. It was this bottom-heavy mass flux profile, attributable to the modification of the thermodynamic environment by repeated cycles of convective development, which was responsible for the reformation of Hermine's low-level vortex and subsequent intensification.

A similar evolution of initially displaced low- and midlevel vortices was seen in the near alignment and RI of Hurricane Dorian (2019; Alvey et al. 2022). Alvey et al. (2022) used a novel analysis of ground-based radar in conjunction with airborne data and reanalysis fields of humidity to show that deep and moderate convection, at least partly driven by terrain interactions with Martinique, led to a repositioning of the low-level vortex closer to the midlevel vortex and in a more humid environment. Further removed from ventilation and in a more nearly aligned state, Dorian commenced RI.

These reformation events suggest that many of the physical processes and relationships between the thermodynamic environment, structure of the precipitation, and kinematic response of the vortex are similar for tropical cyclogenesis and reformation events. Each of the cases described above, however, suffered from a lack of either temporal continuity, high spatial resolution of observations, or deep layers of thermodynamic measurements. Hurricane Sally (2020) was a TC that exhibited many of the characteristics of Hermine (2016) and Dorian (2019): a weak TC in the presence of moderate vertical shear, a midlevel vortex displaced downshear of a low-level vortex, and subsequent convective development, alignment, and RI. Fortunately, this all occurred when Sally was being sampled for a prolonged (approximately 48 h) period by NOAA low- and high-altitude aircraft and close enough to the U.S. coastline to be captured by ground-based radar. The analysis presented here describes the evolution of Sally's thermodynamic environment and inner-core kinematic structure, taking full advantage of the continuous airborne and ground-based observations reaching 14-km altitude. The interaction between the thermodynamic environment, precipitation structure and distribution, and kinematic response of the vortex is documented below.

Thermodynamic conditions govern the structure of the convection, which governs the nature of the mass flux profile, which in turn governs the response of the vortex to the convection. This chain of interactions is applicable both to genesis and (significantly in this case) reformation/alignment and RI onset. What we show in this paper is its applicability to that alignment/RI onset process.

Section 2 describes data and methods used here, while section 3 presents characteristics and time evolution of Sally. The proposed mechanism for vortex alignment is given in section 4 while discussion and conclusions are presented in section 5.

2. Data and methods

To analyze Sally we use high-altitude dropsondes (from the surface to approximately 150–170 hPa) and radar observations from the National Oceanic and Atmospheric Administration's Gulfstream IV, radar observations from WP-3D (P-3) aircraft, the WSR-88D ground radar network, satellite images, and satellite-detected lightning strikes. Here we summarize those datasets.

The data collection shown here was not only contributed by operationally tasked aircraft missions from the NCEP/National Hurricane Center and Environmental Modeling Center, but was also enhanced by the cooperation between researchers from HRD's Hurricane Field Program–Intensity Forecasting Experiment (IFEX; Rogers et al. 2006, 2013; Zawislak et al. 2022) and the Office of Naval Research (ONR) Tropical Cyclone Rapid Intensification (TCRI) field program.

a. High-altitude dropsondes

Overall 134 high-altitude dropsondes were deployed during three (NOAA) Gulfstream-IV (G-IV) flights into Sally. Times on station while deploying dropsondes are specified in Table 1.

Three-dimensional variational analysis (3DVAR) is performed on 129 G-IV dropsondes (5 sondes did not pass the 3DVAR control) to obtain regular grids of data (López Carrillo and Raymond 2011; Raymond and López Carrillo 2011). This resulted in 54 dropsondes in the first flight (Sally1), 56 in the second (Sally2), and 19 in the third (Sally3) flight. In 3DVAR, the penalty function method is applied with an anelastic mass continuity constraint. A 0.25° horizontal and 200-m vertical grid up to 13 km is used. Horizontal smoothing is appropriate for 1° dropsonde spacing, while there is minimal vertical smoothing. Mass continuity is used to calculate the vertical mass flux. Note that no model-derived background field is employed in the 3DVAR analysis.

b. G-IV and P3 radar

Radar observations of the three-dimensional wind field were collected by tail Doppler radars (TDRs) on both the G-IV and P-3 aircraft. The TDRs are X-band, 360° vertically

TABLE 1. Flight time specifies the interval over which dropsondes were deployed. The terms u and v are the assumed storm motion velocity components. Reference time is the time at which the 3DVAR analysis is performed. Dropsonde positions are adjusted to their locations in the storm reference frame at this time.

Case	Flight time and date (UTC)	u (m s^{-1})	v (m s^{-1})	Reference time and date
Sally1	1800 UTC 13 Sep–0100 UTC 14 Sep	−3.8	1.8	2115 UTC 13 Sep
Sally2	0630–1300 UTC 14 Sep	−2.3	1.2	0930 UTC 14 Sep
Sally3	1800–2100 UTC 14 Sep	−2.1	0.9	1930 UTC 14 Sep

scanning radars, which simultaneously scan in cones oriented approximately 20° fore and aft of a plane perpendicular to the heading of the aircraft. Observations undergo an automated quality control process (Gamache 2005) and are mapped onto a Cartesian grid with grid spacing of 2 km in the horizontal and 0.5 km in the vertical. The three-dimensional wind field is retrieved using a variational technique following a similar process to Gao et al. (1999). TDR analyses were created for each TC center pass made by the P-3 or G-IV, as well as select portions of inner-core circumnavigations made by the G-IV. In this, the TC center is identified as the analysis grid point that maximizes the storm-relative tangential wind, which is determined by the application of a cost function that more heavily weights grid points closer to the TC center and those with stronger wind speeds. This TC center-finding process was performed at each radar analysis height following the methods of Fischer et al. (2022).

c. *Ground radar*

Constant altitude plan position indicators (CAPPIs) are constructed using Radx2Grid (Bell et al. 2021) to interpolate elevation angle scans of the reflectivity from Mobile, Alabama (KMOB), Eglin Air Force Base, Florida (KEVX), and Tallahassee, Florida (KTLH), ground radars into 0.5-km vertical and 2-km horizontal resolution Cartesian grids. A composite of the three radars is then constructed by taking the maximum reflectivity value of the three radars at each grid point. In regions of sufficient geometrical radar coverage overlap, the Fast Reorder and Custom Editing and display of

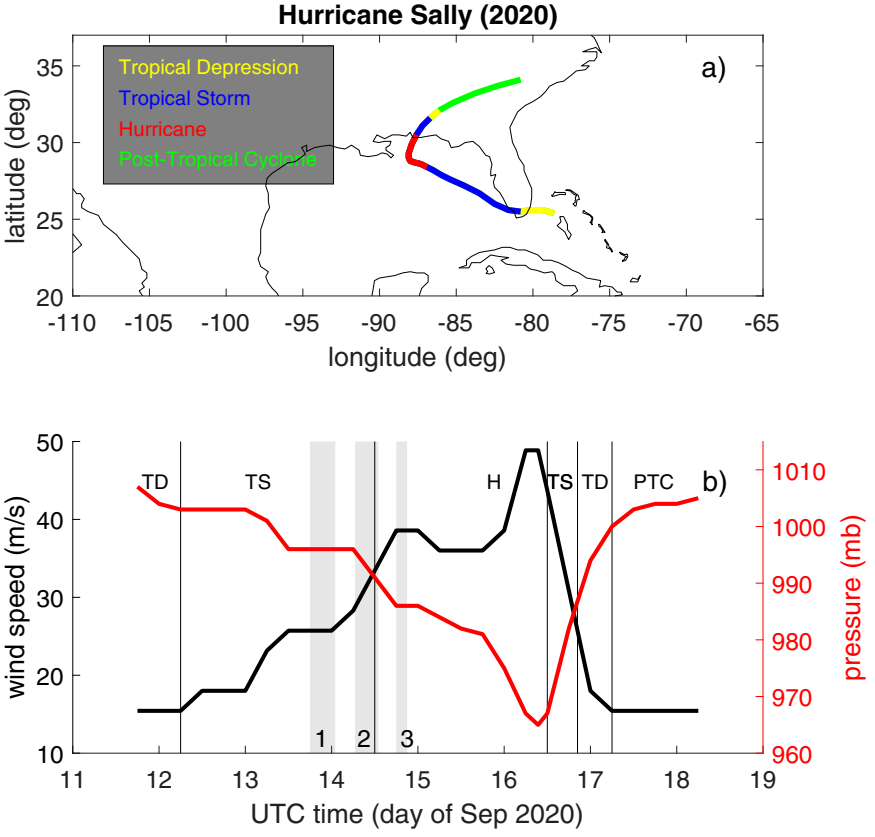

FIG. 1. NHC best track for Sally. TD stands for tropical depression, TS for tropical storm, H for hurricane, and PTC for posttropical cyclone. Gray columns indicate the G-IV flights into Sally, denoted as Sally1, Sally2, and Sally3.

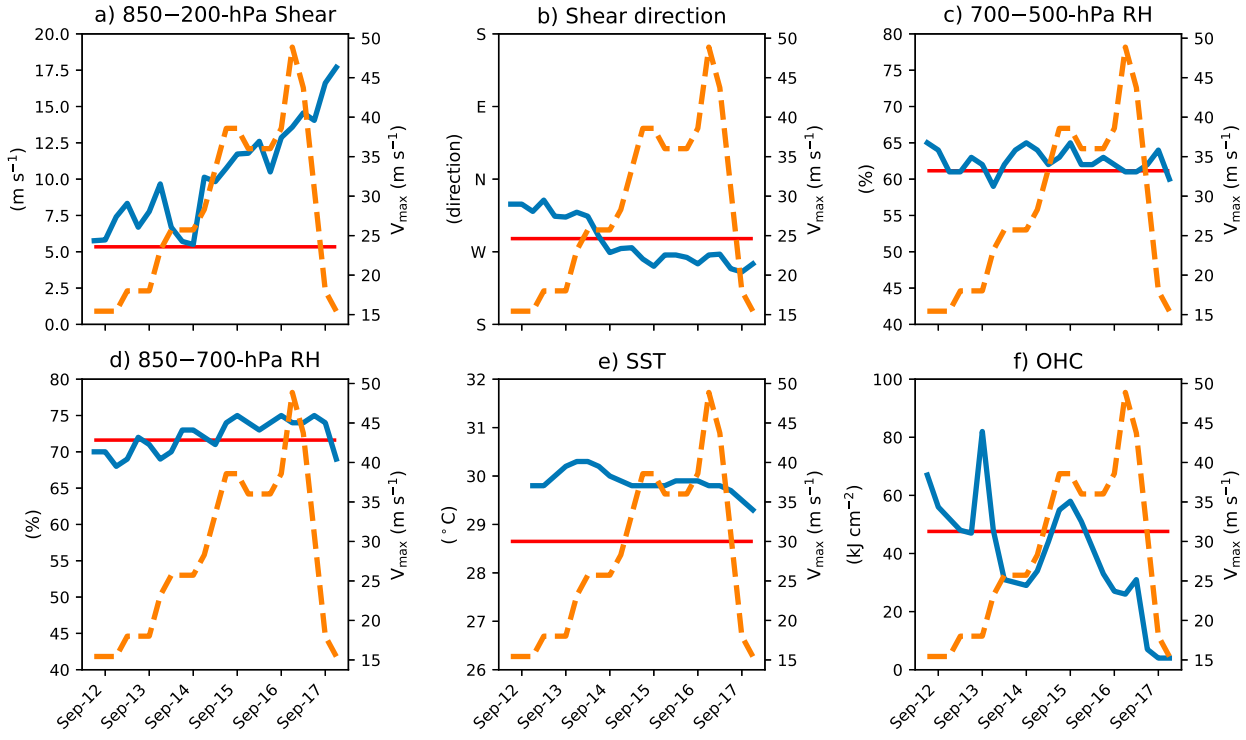

FIG. 2. SHIPS analyses (blue lines) of the (a) 850–200-hPa vertical wind shear magnitude (m s^{-1}), (b) 850–200-hPa vertical wind shear direction (meteorological direction), (c) 700–500-hPa layer-averaged relative humidity (%), (d) 850–700-hPa layer-averaged relative humidity (%), (e) sea surface temperature (°C), and (f) oceanic heat content (kJ cm^{-2}). Analyses span the lifetime of Sally. In some instances, the values of sea surface temperature and oceanic heat content are missing due to the proximity to land. The best track intensity of Sally (m s^{-1}) is shown in the dashed, orange line. The horizontal red lines show the mean environmental value for all RI cases between the years 1982–2020 using the SHIPS database.

Reduced Information in Cartesian Space (CEDRIC) technique is implemented for multi-Doppler wind retrieval (Bell et al. 2021; Razin and Bell 2021). Center locations are identified using the same algorithm as that used for the airborne Doppler data. Because the lowest elevation angle scan of the radars is at 3–4-km altitude near Sally, low-level center locations could not be identified from the ground radars. Instead, low-level center locations are determined by interpolating between Air Force Reconnaissance flight-level center fixes (1.5–3-km altitude) and TDR analysis centers. Similar to Rogers et al. (2020), precipitation types are delineated using the CAPPIs and a modified Steiner et al. (1995) algorithm as outlined in Alvey et al. (2022). Precipitation is first characterized as either stratiform or convective using the 3–4-km CAPPIs within 250 km and 6-km CAPPIs for radii > 250 km. Convective pixels are further categorized using the 20-dBZ echo top height as either shallow (<6.5 km), moderate (6.5–10 km), or deep (>10 km).

d. Satellite

Infrared (IR) satellite brightness temperatures were obtained from the global merged geostationary satellite infrared brightness temperature (Tb) dataset (Janowiak et al. 2017), which features globally gridded satellite observations with a horizontal resolution of approximately 4 km every 30 min. For figures combining IR brightness temperatures with TDR analyses, the IR observation time nearest to the TDR analysis time was selected.

We also use time series of Geostationary Lightning Mapper (GLM) detected flash counts.

3. Characteristics of Sally

a. Synoptic scale

Figure 1 shows the best track position and intensity for Sally from the NOAA National Hurricane Center (NHC) TC Report, while Fig. 2 shows Statistical Hurricane Intensity Prediction Scheme (SHIPS) analyses of key environmental parameters and the best track intensity during the lifetime of Sally.

Sally formed from a trough axis that moved through the Bahamas, where it was declared a tropical depression by the NHC near the coast of southeast Florida at 1800 UTC 11 September (Berg and Reinheart 2021). Sally continued tracking west-northwest into the southeastern Gulf of Mexico over the next several days. Moderate northwesterly shear [Rios-Berrios and Torn (2017) define it as ranging from 4.5 to 11 m s^{-1}] prevented substantial strengthening of Sally (Fig. 2b) as it moved northwestward, but that shear decreased as deep convection

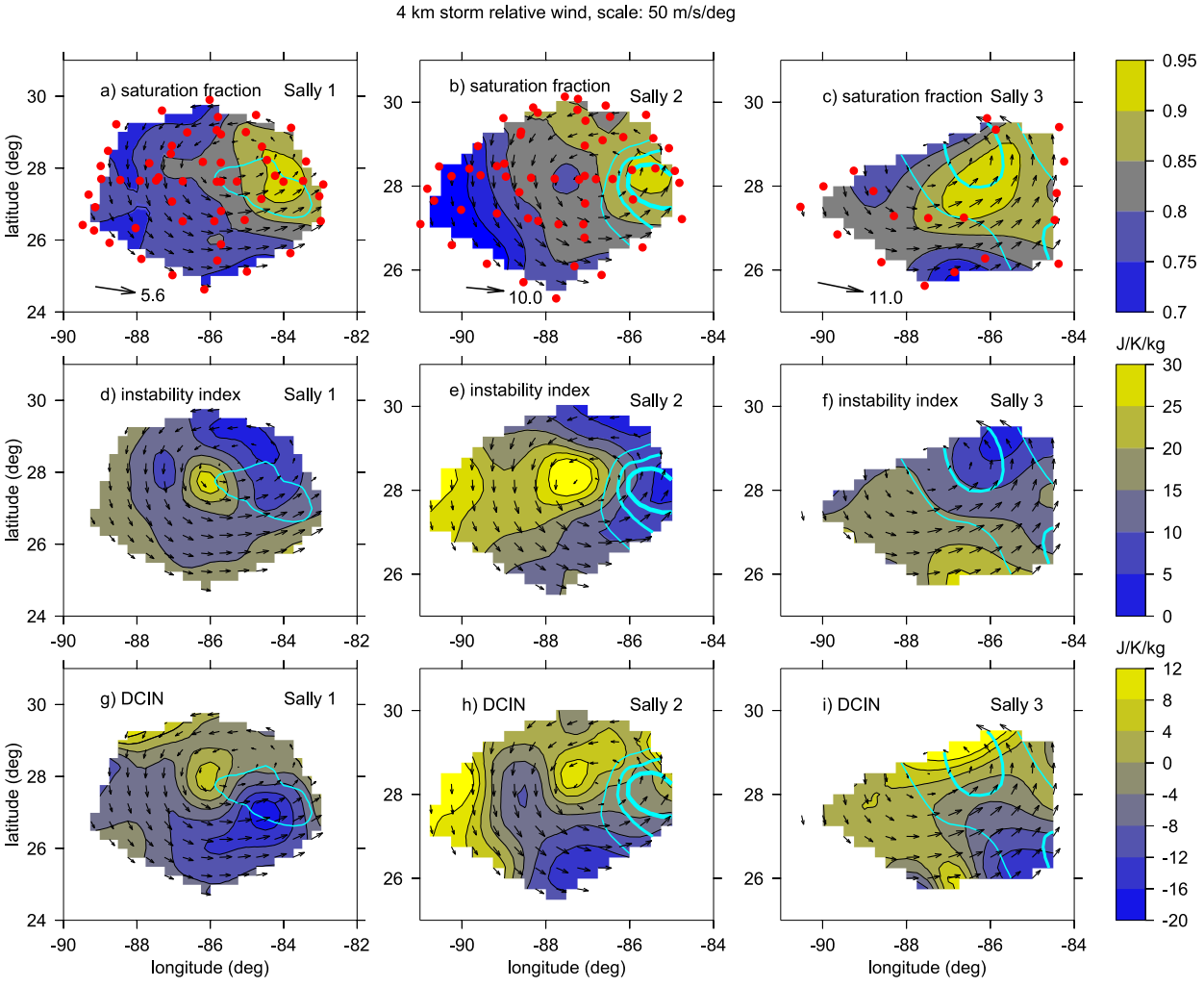

FIG. 3. (left) Sally1, (center) Sally2, and (right) Sally3: (a)–(c) saturation fraction, (d)–(f) instability index, and (g)–(i) DCIN. The 4-km vertical mass flux is given in cyan (from 0.1 kg m^{-2} s^{-1}, with 0.1 kg m^{-2} s^{-1} increments) in all panels. The arrows show 4-km storm relative winds. Red dots in(a)–(c) show location of dropsondes. The deep-layer shear vectors (m s^{-1}) are shown in (a)–(c) at the bottom left of each panel.

developed east of the low-level center, during which time Sally underwent a brief period of RI about 200 km south of the Florida Gulf Coast on 14 September. Sally's peak winds increased by 20 kt (1 kt ≈ 0.51 m s^{-1}) on 14 September over the 12-h period from 0600 to 1800 UTC. Shear then increased again, limiting further intensification. A second brief period of RI marked by enhanced upper-level divergence occurred just prior to landfall along the Alabama Gulf Coast. We acknowledge Sally did not satisfy the RI definition introduced in Kaplan and DeMaria (2003), nevertheless, the observed intensification rate did satisfy the 25 kt in 24 h and 20 kt in 12 h RI definitions examined in Kaplan et al. (2010, 2015). Sally was sampled by NOAA and Air Force aircraft during much of this period, including a set of three missions by the G-IV aircraft prior to and during the first RI period (Fig. 1b). Dropsonde and tail Doppler radar data from these G-IV missions and a P-3 mission will be examined here, as will flight-level data from the Air Force C-130s, ground-based radar along the Gulf Coast and GOES satellite images. These datasets and the analyses arising from them were described in the section above.

The SHIPS analysis environmental parameters from Fig. 2 show that deep-layer shear steadily increased to >10 m s^{-1} between 13 and 15 September, the time of the initial RI period and aircraft missions examined here. Although shear of this magnitude is stronger than the environmental shear of the typical RI case (Fig. 2a), SHIPS analyses show Sally was in a favorable synoptic-scale environment from a thermodynamic perspective. Both midlevel (Fig. 2c) and low-level (Fig. 2d) relative humidity were near or above the mean values of RI cases during Sally's intensification. Additionally, Sally was over warm waters with sea surface temperatures approximately 1°C higher than mean value for RI cases (Fig. 2e), and oceanic heat content similar to the mean value observed during RI (Fig. 2f).

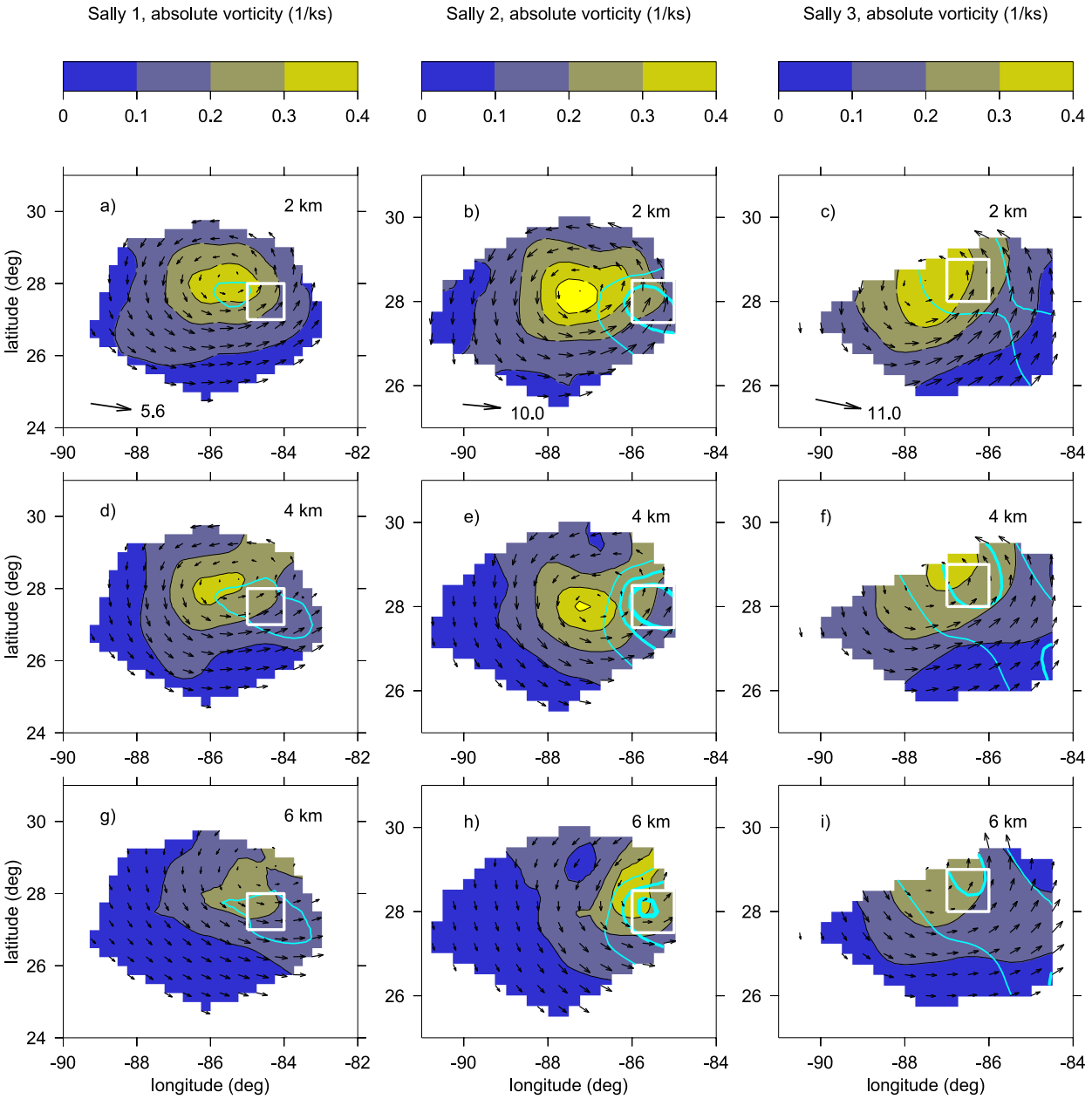

FIG. 4. Absolute vorticity (ks^{-1}) in blue/yellow contours at (a)–(c) 2, (d)–(f) 4, and (g)–(i) 6 km. The vertical mass flux is given in cyan (from 0.1 kg m^{-2} s^{-1}, with 0.1 kg m^{-2} s^{-1} increments) at the same levels. White boxes indicate the area of the strongest vertical mass flux at 4 km. Velocity vectors are scaled as in Fig. 3. The shear vectors (m s^{-1}) are shown in (a)–(c) at the bottom left of each panel.

b. Mesoscale structure and evolution

Here we look at the mesoscale structure and evolution as described by the thermodynamic variables from the introduction, including the saturation fraction, the instability index and DCIN, as well as the absolute vorticity and vertical mass flux from the 3DVAR from high-altitude dropsondes described in the previous section. The results presented here are in the storm moving reference frame with storm velocities u and v given in Table 1 obtained from the NHC TC Report. Since dropsondes are deployed at different times, their positions are adjusted to their locations relative to the moving disturbance before incorporation into the 3DVAR analysis.

The first G-IV flight into pre-Hurricane Sally (Sally1) deployed dropsondes from 1800 UTC 13 September to 0100 UTC 14 September. The second flight (Sally2) deployed dropsondes from 0630 to 1300 UTC 14 September and the third and final G-IV flight into Sally (Sally3; now a hurricane) deployed dropsondes from 1800 to 2100 UTC 14 September.

Figure 3 shows the patterns of saturation fraction, instability index and deep convective inhibition for Sally1, Sally2 and Sally3. Superimposed in Figs. 3a–c are red dots indicating the locations of dropsondes. The arrows show 4-km storm relative winds. Overlapped over saturation fraction and instability index in cyan is the 4-km vertical mass flux, a good proxy for convection. Figure 4 shows patterns of absolute vorticity and vertical mass flux at 2, 4, and 6 km for these cases. Comparison of these figures illustrate the relationships between the patterns of mass flux, absolute vorticity, and thermodynamic variables.

For Sally1, Fig. 3 shows that large values of saturation fraction are spread broadly over the region of strongest upward mass flux at 4 km, an indicator of area of strong convection, which is located in the eastern part of the domain. We see that the strongest mass flux occurs south-east of the smallest instability index, where values range from 10 to 15 J K^{-1} kg^{-1}, in the downshear portion of the storm. The largest values of instability index nearly coincide with the largest values of DCIN in the area that is generally free of convection. The lowest values of DCIN occur upstream of the region with strong mass fluxes. This is consistent with the idea that convective cells are initiated in regions of low DCIN, which then advect with the flow into the region of strongest mass fluxes. The 2- and 4-km absolute vorticity maxima are approximately aligned, but the weaker 6-km vortex is somewhat ill-defined and is generally located to the northeast of the lower-level vortices (Fig. 4) or downshear-left of the low-level center (Fig. 2). This configuration is consistent with the preferred shear-relative tilt orientation from previous climatological observational studies (Reasor et al. 2013; Fischer et al. 2022).

In Sally2, the strong convection is also in the east part of the domain, where large saturation fraction and small instability index are collocated with strong mass flux at 4 km. The strongest mass flux also occurs where the instability index ranges from 10 to 15 J K^{-1} kg^{-1}. The lowest values of DCIN occur upstream of the region with strongest mass fluxes, as in Sally1. Figure 4 shows significantly stronger maximum vertical mass flux in Sally2 than in Sally1. The absolute vorticity maxima at 2 and 4 km are also stronger in Sally2 and are located 150 km to the west of the strong convection. However, the 6-km vorticity maximum is collocated with the convection.

In Sally3 we see that large values of saturation fraction are spread broadly over the maximum vertical mass flux, as in the earlier cases. Convection is collocated with small values of instability index as well. The lowest values of DCIN occur in the southeast quadrant, upstream of the region with strong mass fluxes, as in Sally1 and Sally2. However, unlike the earlier cases, the vorticity maxima at all three levels are nearly aligned (Fig. 4). The maximum vertical mass flux is located at the east edge of the region of strong 6-km absolute vorticity.

Figure 5 shows the vertical mass flux profiles for the Sally observational periods, averaged over degree by degree white boxes, selected to coincide with the location of peak 4-km mass flux, shown in Fig. 4. Sally2 exhibits the strongest vertical mass fluxes, but all profiles are bottom heavy with maximum vertical mass flux at 4–5-km altitude.

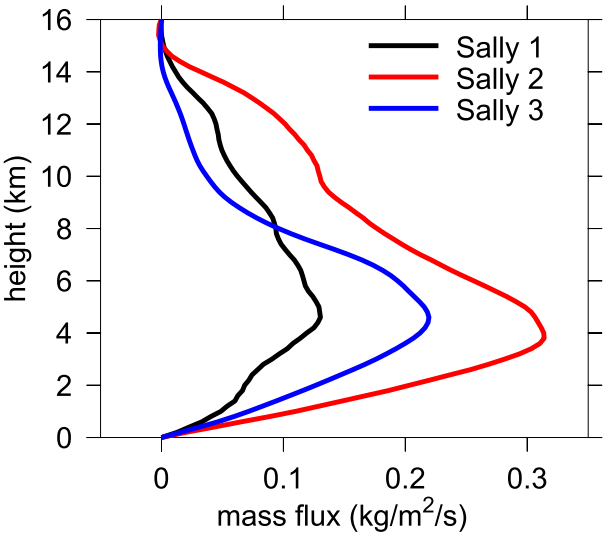

FIG. 5. Vertical mass flux profile averaged over the white boxes from Fig. 4 for Sally1, Sally2, and Sally3.

In all three cases the strongest mass fluxes occurred to the east or southeast of the 2-km circulation center, consistent with preferentially downshear convection (Corbosiero and Molinari 2002), and was nearly collocated with the 6-km absolute vorticity maximum, especially for Sally2 (Fig. 4). This supports the hypothesis that the midlevel vortex favors the formation of strong convection with a bottom-heavy mass flux via its effect on decreasing the instability index.

Figure 6 shows the averaged absolute vorticity vertical profiles within the region of strongest mass flux (in red) noted by white boxes in Fig. 4 and over the 1° box covering the center of low-level circulation (in blue) for Sally1, Sally2, and Sally3 for comparison. Figure 6 tells us two important things. First that in the area of convection, the absolute vorticity peak at 6 km is well defined for Sally2, while that is not the case in Sally1. Together with the strong bottom-heavy vertical mass flux that occurred in Sally2, this sets favorable conditions for RI (Raymond et al. 2014; Rogers et al. 2020). In Sally3 the absolute vorticity is strong at levels below 6 km as by that time the vortices have aligned. The second thing that we learn from this figure is that if we look only at the absolute vorticity profiles centered around the low-level circulation center, we lose an important piece of the puzzle, which is the importance of the presence of a midlevel vortex.

The importance of the midlevel vortex is also illustrated by airborne and ground-based radar observations discussed in the next section.

c. *Convective-scale evolution during vortex reformation*

As described in the previous subsection, the mass flux at 4-km altitude, which is a proxy for convective strength, was at its strongest during the Sally2 mission. It was during this mission that Sally underwent a dramatic evolution, organizing from a misaligned, asymmetric weak tropical storm into an aligned, rapidly intensifying hurricane over a matter of hours. This section will document this evolution, focusing on the

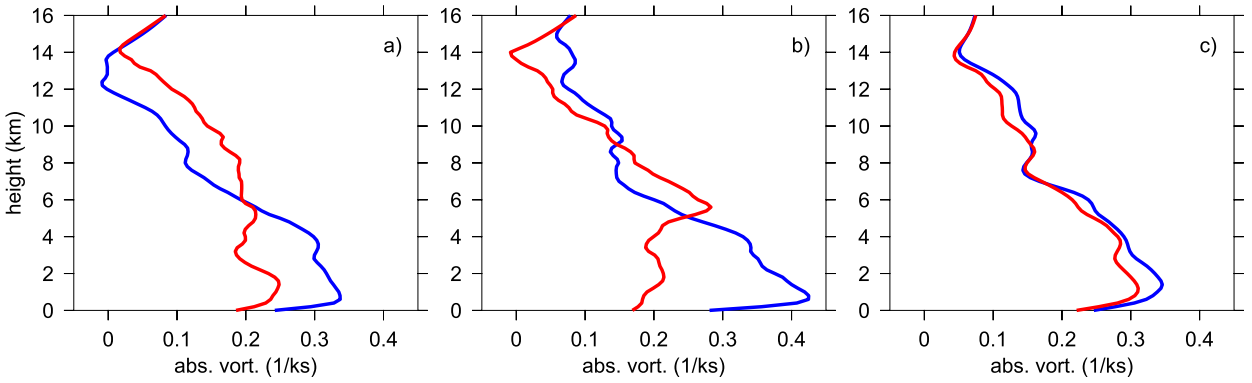

FIG. 6. Absolute vorticity vertical profiles averaged over the white boxes from Fig. 4 in red and averaged over the center of the low-level circulation in blue for (a) Sally1, (b) Sally2, and (c) Sally3.

kinematic and precipitation structure and evolution during Sally2 and how those changes were related to Sally's alignment and intensification.

Snapshots of satellite imagery show the convective evolution beginning from late on 13 September through 14 September (Fig. 7). Initially, the convective structure of Sally is asymmetric, with the coldest IR brightness temperatures and lightning activity displaced to the east (downshear; Fig. 2b) of the low-level TC center (Figs. 7a–d). After approximately 0900 UTC there is a significant decrease in the minimum IR brightness temperatures and an areal expansion of temperatures $< -70^{\circ}$C, consistent with an increase in convective activity. This convective activity occurs near the location of the 6-km TC center position identified from ground radar velocities (Fig. 7d).

By 1300 UTC, near the end of Sally2, GLM-detected lightning activity had dramatically increased within 100 km of the 6-km TC center (cyan markers in Fig. 7f). The large increase

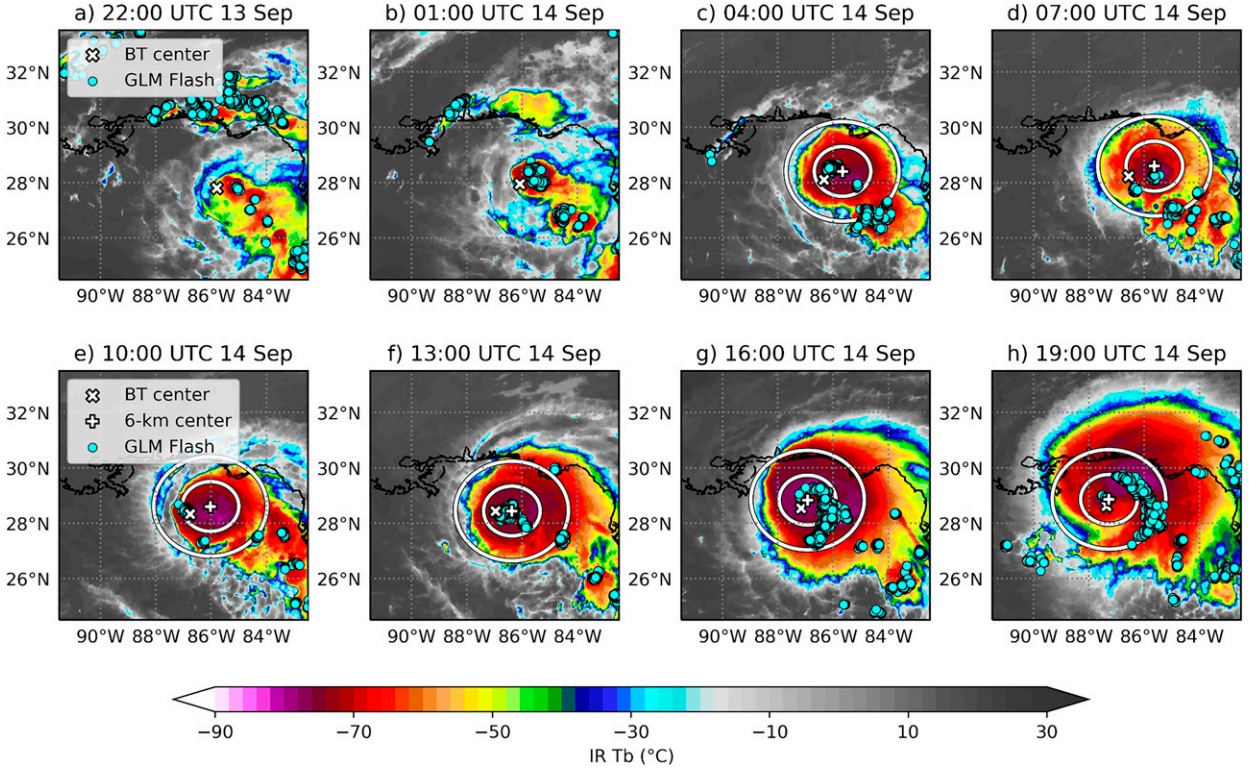

FIG. 7. (a) IR brightness temperatures (°C; shaded) at 2200 UTC 13 Sep. The interpolated best track position is shown by the white "X," the ground-radar derived TC center at a height of 6 km is shown by the white "+," and all GLM-detected lightning flashes within ±15 min of the IR image are shown by the cyan circles. White radial rings are shown at 100 and 200 km from the 6-km circulation center. (b)–(h) As in (a), but for analyses over the next 21 h (through 1900 UTC 14 Sep), shown every 3 h.

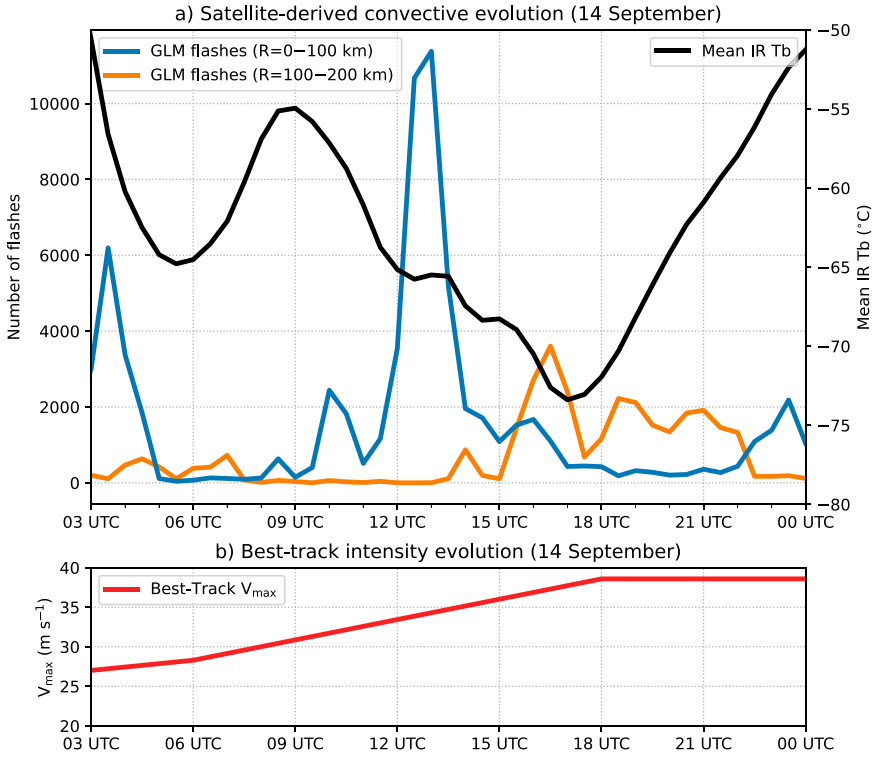

FIG. 8. (a) Time series of GLM-detected flash counts over event-centered 30-min intervals within 0–100 km (blue line) and 100–200 km (orange line) from the TC center at a height of 6 km during 14 Sep. Time series of the area-averaged IR brightness temperatures (°C) within 200 km of the 6-km TC position over the same period is shown by the black line. (b) The corresponding best track intensity evolution (m s^{-1}) for the same period shown in (a).

in lightning activity and decrease in area-averaged IR brightness temperatures around this time are more evident in the time series shown in Fig. 8a. Over a 2-h period between 1100 and 1300 UTC, the 30-min total flash count increased about tenfold, from just under 1000 to over 11 000. This evolution suggests that a significant convective burst occurred near the midlevel TC center during that time interval. Thereafter, the IR signature became increasingly symmetric, with an enhancement of relatively low IR brightness temperatures left of shear and upshear of the interpolated best track position (Figs. 7d–f), as Sally experienced a period of rapid intensification (Figs. 1 and 8b).

Interestingly, the 6-km TC center position prior to the time of the convective burst (Figs. 7a–f) was consistently displaced downshear of the TC surface center, as estimated from best track. The tilted nature of the TC vortex is consistent with the variational analyses shown in Fig. 4. By 1600 UTC 14 September, however, the vortex becomes better aligned (Figs. 7g,h).

To further examine the vortex structural change over this period, Fig. 9 shows a series of TDR analyses from successive G-IV and P3 missions into Sally. Consistent with the variational analysis from Sally2, Figs. 9a and 9d indicate a pronounced misalignment of the lower-tropospheric and midtropospheric circulation centers at 0645 UTC. Although insufficient coverage precluded an objective TC center estimate at a height of 2 km, there are no signs of a closed circulation at a height of 2 km beneath the location of the objectively identified 6-km TC center. The south-southeasterly winds at 2 km beneath the location of the midlevel vortex suggest that any lower-tropospheric circulation was displaced significantly westward of the midlevel center, consistent with Fig. 7d. Two hours later, an additional G-IV TDR analysis at 0840 UTC showed increased cyclonic curvature of the 2-km wind field beneath a closed circulation in the midlevels (Figs. 9b,e), although there are no obvious signs of a closed lower-tropospheric circulation beneath the midlevel vortex location at this time. Following an approximate 7-h gap between available TDR analyses, the next analysis revealed a substantial change in vortex structure by 1540 UTC (Figs. 9c,f). Not only had the vortex become better aligned in the vertical, but the vortex had rapidly intensified. For instance, the maximum 2-km wind had increased by approximately 20 m s^{-1} between the 0840 and 1540 UTC TDR analyses. Although it is possible that the strongest winds were not sampled in the G-IV TDR analyses in Fig. 9, a sharp uptick in winds and an 11-hPa decrease in central pressure were observed by an Air Force reconnaissance mission flying at a height of approximately 1.5 km between 1200 and 1600 UTC, which also indicate that Sally experienced a brief period of substantial intensification. Despite the temporal gaps in coverage, the TDR analyses demonstrate that Sally became increasingly aligned and rapidly intensified

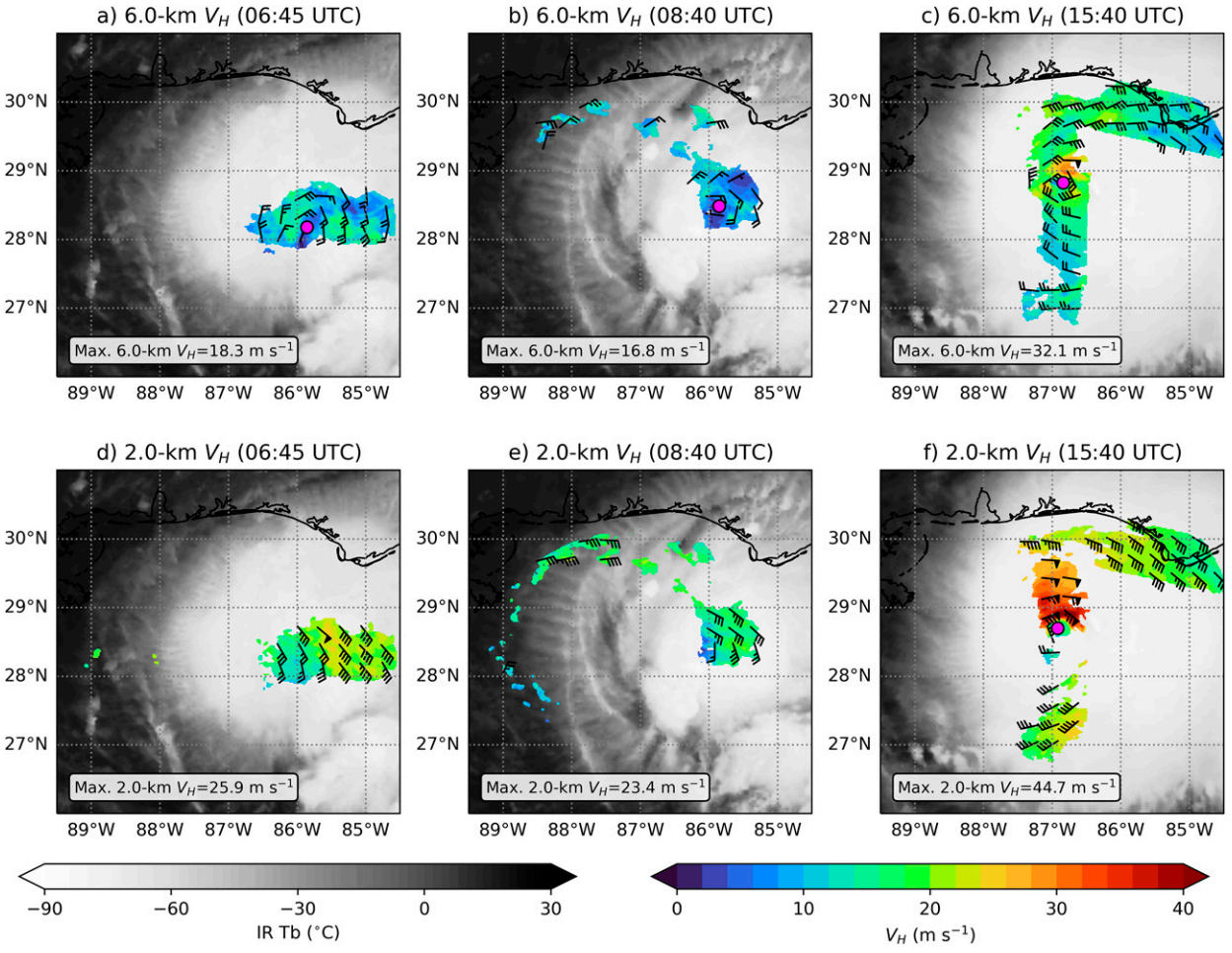

FIG. 9. (a) G-IV TDR analysis of 6-km Earth-relative wind (color shading and barbs) at 0645 UTC 14 Sep from the 20200914N1 (Sally2) mission. Coincident IR brightness temperatures (°C) are shown by the grayscale shading. The maximum 6-km wind speed is displayed by the text within the box at the bottom left of the panel. (b) As in (a), but for a G-IV TDR analysis at 0840 UTC 14 Sep. (c) As in (a) and (b), but for the first P3 TDR analysis from the 202009I1 mission at 1540 UTC 14 Sep. (d)–(f) As in (a)–(c), but for TDR analyses at a height of 2 km. For each panel, the objectively identified TC center at the respective height is shown by the magenta circle, provided sufficient data coverage exists.

during a period when there was intense convective activity (Figs. 7 and 8).

While the aircraft missions described above had a substantial temporal gap during Sally's alignment, multi-Doppler wind retrievals from KEVX, KMOB, and KTLH land-based radars provide the ability to examine the relationship between the TC convective structure, vortex misalignment, and intensification during this gap in TDR coverage. The distance of the TC from the radar sites precludes analyses of the lower-tropospheric vortex and precipitation structure. However, the combination of 6 km AGL tangential wind and storm-relative centers from the radars and the positions of flight-level Air Force reconnaissance lower-tropospheric center fixes is illuminating.

Figure 10 shows the position of the low-level center (LLC, 1.5 km AGL) and midlevel circulation (MLC, 6 km AGL) during a 14-h period spanning Sally's alignment, while Fig. 11 shows time series of vortex tilt and precipitation mode from the ground radar. At 0300 UTC 14 September a reconnaissance aircraft fixed the LLC approximately 70 km from the 6-km midlevel circulation (MLC), as shown in Fig. 10a. This downshear tilted nature of the TC vortex is consistent with the variational analyses shown in Fig. 4. Deep convection observed from 0000 to 0300 UTC is followed by a rapid increase in the stratiform precipitation coverage from 30% to 70% from 0300 to 0630 UTC (Fig. 11b), which also coincides with the time period between Sally 1 and Sally 2 during which an amplification and deepening of the midlevel vortex is identified (Figs. 6 and 11a). Following the peak of stratiform precipitation (0700 UTC), the kinematic organization of the MLC slightly deteriorates (Fig. 10b), the depth and strength of mid- to upper-level vorticity (Fig. 11a) slightly decreases, and the displacement from the LLC increases (Figs. 11a,b). However, deep convection redevelops by 0900 UTC within 50 km of the

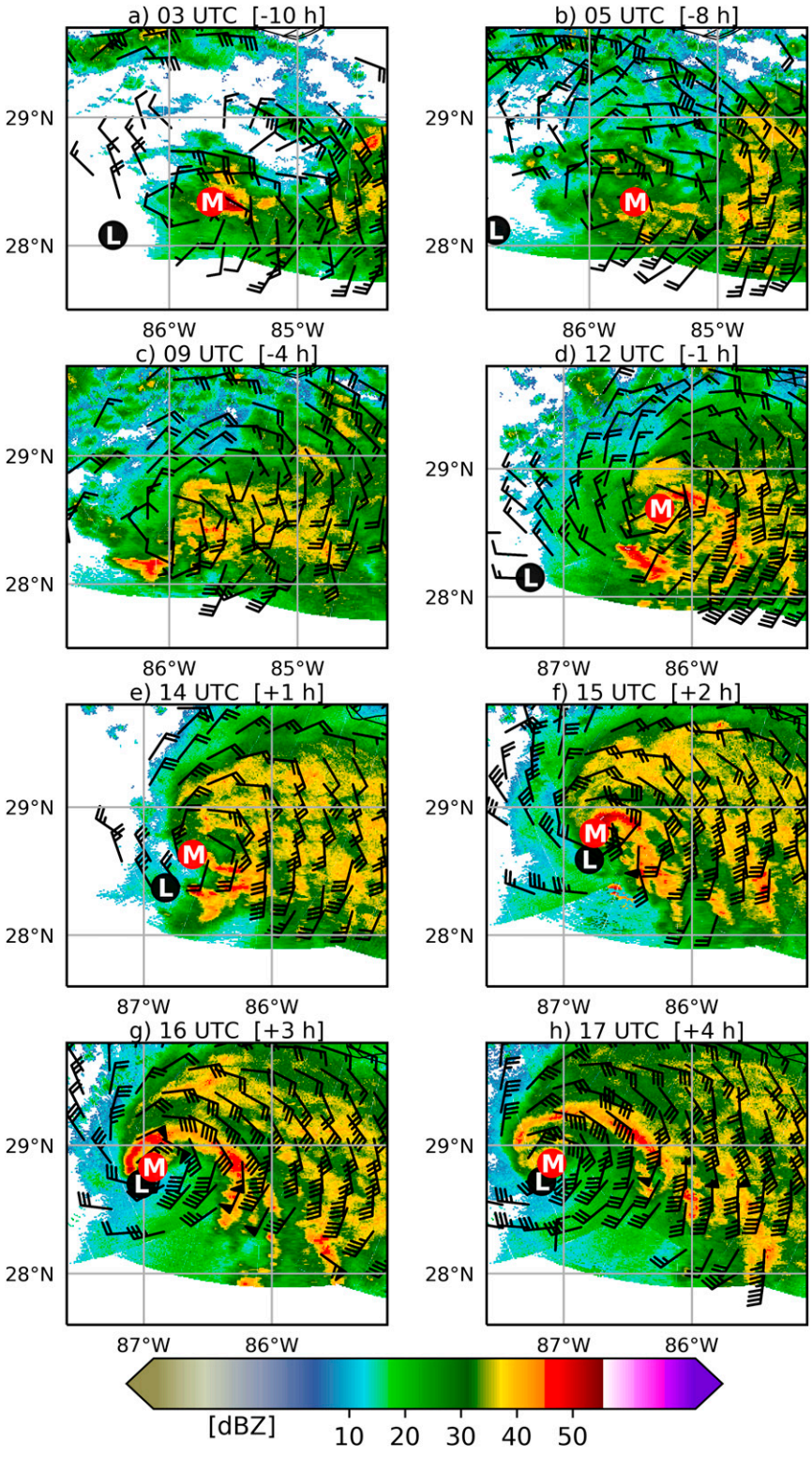

FIG. 10. (a)–(h) Reflectivity (color fill) at 4 km AGL from ground based radar and 6 km AGL storm-relative wind (barbs) derived using Fractl on 14 Sep. Reformation-relative times are indicated in brackets. Red circles ("M") indicate 6-km centers and black circles ("L") denote low-level aircraft reconnaissance center fixes for all times except 0900 UTC [in (c), because an objective center estimate could not be determined].

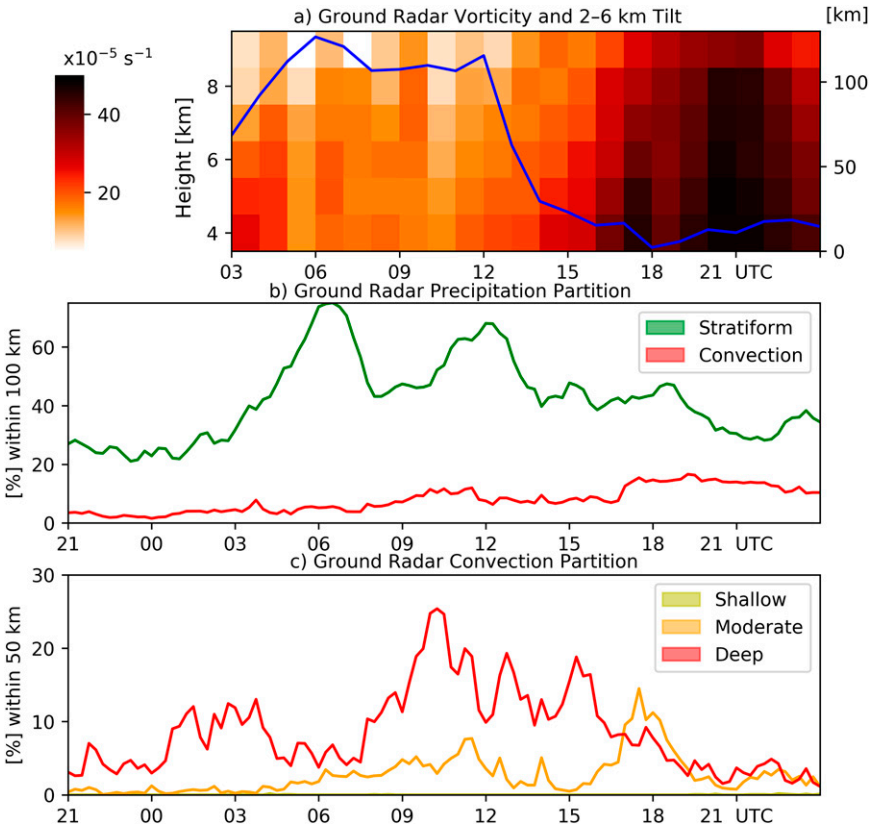

FIG. 11. (a) Hovmöller/plot with respect to height of relative vorticity (color shading) averaged within 100 km of the midlevel center using ground based radar multi-Doppler wind retrievals on 14 Sep. Vortex tilt is calculated as the distance between the 2–6-km (blue line) centers. (b) The percent areal coverage for partitions of stratiform (green) and convection (red) within 100 km of the 6-km center using a composite of KEVX, KMOB, and KTLH radars on 13–14 Sep. (c) The percent areal coverage of shallow convection (yellow), moderate convection (orange), and deep convection (red) within 50 km of the 6-km center.

MLC center (Fig. 11c) and significantly increases in strength and areal coverage through 1600 UTC. Furthermore, the separation between the low-level and midlevel vortex centers decreases dramatically between 1200 and 1600 UTC from in excess of 100 km to about 20 km, bringing them into near alignment.

The vorticity of the MLC increases rapidly from $\sim 20 \times 10^{-4}$ to $>30 \times 10^{-4}$ s^{-1} after 1200 UTC, as seen in Fig. 11a. This increase is most likely due to the intensified convection near the MLC core. Midlevel vorticity continues to rapidly increase in the period from 1600 to 1900 UTC from 30×10^{-4} to $>50 \times 10^{-4}$ s^{-1} in the 4–9-km vertical layer.

The combination of increased coverage of both moderate and deep convection around the MLC prior to and during alignment (Fig. 11c) is similar to what was seen in Hermine (2016, Rogers et al. 2020).

4. Mechanism of vortex alignment

As shown during the Sally2 mission, Sally underwent a significant structural evolution, with the low and midlevel vortices becoming aligned over a short (~3 h) time period. There have been several studies that have looked at what causes this alignment for weak tropical cyclones (e.g., Nguyen and Molinari 2015; Rogers et al. 2020; Schecter and Menelaou 2020). Nguyen and Molinari (2015) and Rogers et al. (2020) emphasize stretching, and to a lesser extent tilting, as mechanisms leading to vortex alignment. Schecter and Menelaou (2020) investigate the role of the irrotational velocity field in vertically aligning the vortex of a simulated tropical cyclone with initially misaligned circulations at low and midlevels. In their analysis, they split the horizontal wind field into solenoidal and irrotational parts. Without the primary part of the irrotational flow, which is mostly produced by convection, this alignment does not occur. They do not split the horizontal flux of absolute vorticity into advective and stretching parts, so it is hard to tell from their analysis whether advection simply moves the low-level vortex toward the upper-level vortex or whether stretching by convection causes regeneration of the low-level vortex there. Nevertheless, their analysis shows that dry adiabatic flows, which are mostly solenoidal, are unable to produce the alignment observed in their simulation; convectively induced irrotational

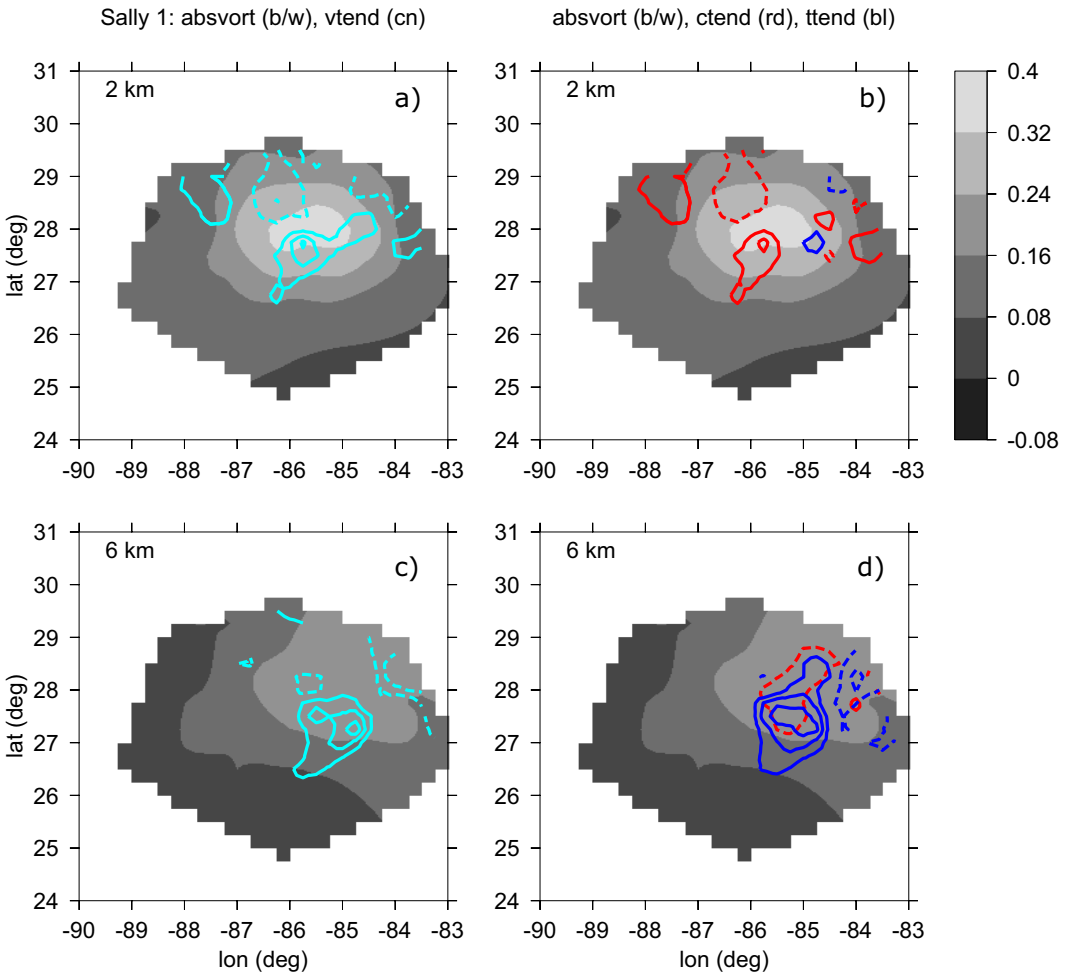

FIG. 12. Sally1: (a),(c) Absolute vorticity (grayscale; ks^{-1}) and total vorticity tendency (vtend; cyan), and (b),(d) its components vorticity convergence tendency (ctend; red) and tilting tendency (ttend; blue). Patterns at (top) 2 and (bottom) 6 km are shown. The contour interval for all tendencies is 0.006 ks^{-2} with solid and dashed contours indicating positive and negative values, respectively. Zero contours are omitted.

flows linked to vertical convective motions by mass continuity are needed.

The development of the simulated cyclone of Schecter and Menelaou (2020) with its rapid final alignment phase bears a strong resemblance to Sally's behavior. As noted in section 3c, the low-level vortex in Sally appeared to move into alignment with or reform underneath the midlevel vortex in only a few hours, preceded by a long period in which the low-level vortex actually moved away from the midlevel vortex. This realignment occurred toward the end of the Sally2 observational period (Fig. 11 and Table 1). Thus, Sally2 dropsondes and surface and airborne radar observations fortuitously captured the strong convection associated with the alignment of the vortex column in Sally. As Figs. 4 and 5 show, the vertical mass flux in Sally2 was significantly stronger than in Sally1 and Sally3.

As discussed in section 1, (5) and (6) govern the time tendency of the vorticity field in a tropical cyclone, given the velocity field. Figures 12a,c, 13a,c, and 14a,c show the absolute vorticity (gray shading) and the total vorticity tendency (cyan contours) at 2 and 6 km, derived from the dropsonde analyses for the 3 Sally cases. Figures 12b,d, 13b,d, and 14b,d show the absolute vorticity as well as the components of the total tendency, including that due to absolute vorticity convergence $-\nabla_h \cdot (\mathbf{v}_h \zeta_z)$ (red contours) and tilting $\nabla_h \cdot (\boldsymbol{\zeta}_h w_z)$ (blue contours).

As Fig. 12 shows, maximum total vorticity tendency at 2 km in Sally1 occurs near 27.5°, −85.8° while the 6-km maximum occurs further east near 27.5°, −84.8°. In agreement with the mass flux profile for Sally1 (Fig. 5), which shows increasing mass flux with height below 4 km, implying mass convergence, the total tendency there is dominated by positive vorticity convergence, though there is a weak positive contribution from tilting as well. In contrast, at 6 km the mass flux decreases with height, resulting in mass divergence and corresponding vorticity divergence. However, this negative tendency is overcome by a strong positive tendency due to tilting. At both 2 and 6 km, the maximum tendencies are located to the south of the existing absolute vorticity maximum.

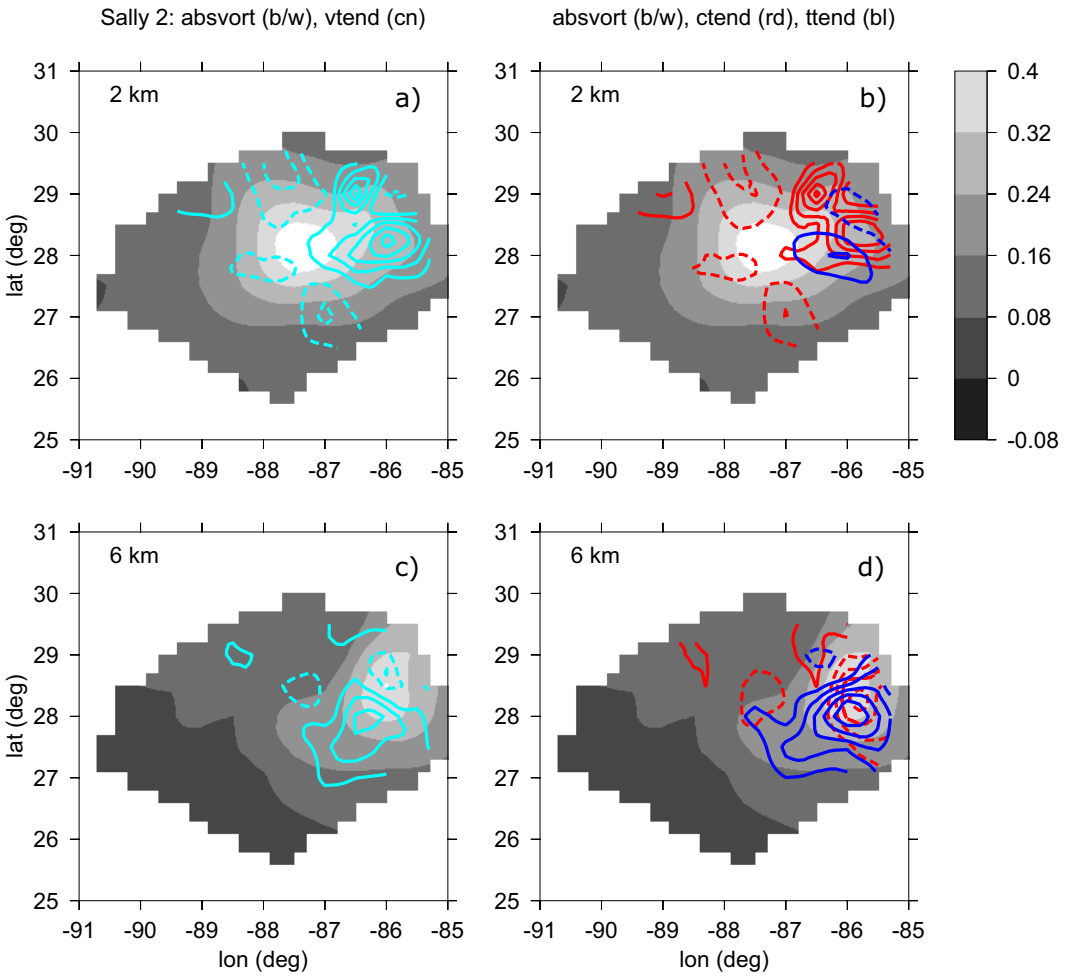

FIG. 13. As in Fig. 12, but for Sally2.

In Sally2 (Fig. 13) the vertical mass flux is nearly 3 times that seen in Sally1, with corresponding increases in both convergence and tilting tendencies. As in Sally1, convergence dominates at 2 km while tilting dominates at 6 km. However, unlike Sally1, the maximum 2-km tendency is located about 1.5° to the east of the existing vorticity maximum. Given the maximum magnitude of approximately 0.03 ks^{-2} for the 2-km tendency, this would lead to the regeneration of the 0.4-ks^{-1} vorticity maximum at 2 km in its new location in approximately 13 ks = 3.6 h. This regenerated vortex would be located slightly to the south of the preexisting 6-km vortex in the direction of the maximum 6-km vorticity tendency. The eastward reformation of the 2-km vortex plus the slight southward reformation of the 6-km vortex can therefore explain the observed rapid alignment of the vortices at the two levels into a single vertical column.

The strong positive vorticity tendency at 6 km in Sally2 due to tilting is a bit of a surprise, in that it is sufficient to overcome the negative stretching tendency at this level that comes from the decrease in mass flux with height there. This means that a top-heavy mass flux profile with mass flux increasing with height at midlevels and associated positive stretching is not needed to spin up a midlevel vortex as long as a sufficiently strong tilting tendency exists. In Sally2 this tendency comes from the combination of upward motion and strong anticyclonic vertical shear of the horizontal wind.

Examination of Fig. 14 shows that the vertical alignment of the 2- and 6-km vortices has been maintained in Sally3. Furthermore, the maximum 2-km vorticity tendency, due to strong vorticity convergence and a weak positive tilting contribution, is nearly aligned with the vortex column, implying rapid strengthening of the vortex at this level. At 6 km the vorticity convergence and tilting contributions nearly cancel at the vorticity maximum, though there appears to be a positive tendency somewhat to the east of the maximum. Subsequently Sally underwent additional rapid intensification, but detailed dropsonde measurements were not available at that point.

The vorticity convergence tendency may be decomposed into stretching and advective tendencies:

$$-\nabla_h \cdot (\mathbf{v}_h \zeta_z) = -\zeta_z \nabla_h \cdot \mathbf{v}_h - \mathbf{v}_h \cdot \nabla_h \zeta_z. \quad (7)$$

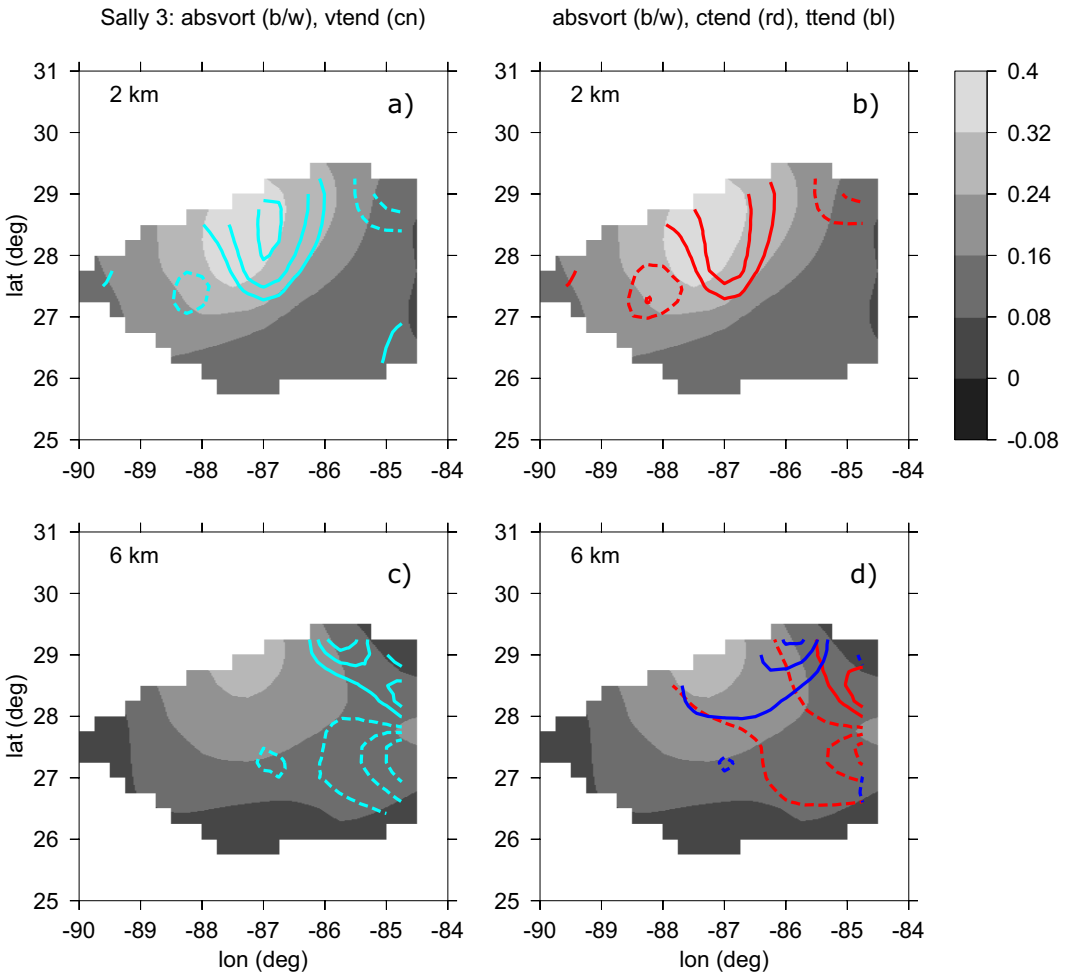

FIG. 14. As in Fig. 12, but for Sally3.

As an example, Figs. 15a and 15b show this decomposition at 2 and 6 km for Sally2. Both terms contribute significantly to the vorticity convergence tendency. The advective tendency at 2 km reflects the effect of the cyclonic circulation around the vorticity maximum at that level but does not contribute significantly to the alignment of the vortex column, which is accomplished primarily by stretching at this level according to the Sally2 3DVAR analysis.

Similarly, the Eulerian tilting tendency may be decomposed into Lagrangian tilting and vertical advection of vorticity:

$$\nabla_h \cdot (w\boldsymbol{\zeta}_h) = \boldsymbol{\zeta}_h \cdot \nabla_h w - w\frac{\partial \zeta_z}{\partial z}, \tag{8}$$

where $\nabla \cdot \boldsymbol{\zeta} = 0$ has been used. Figures 15c and 15d show the Eulerian tilting term as well as the tendency due to the vertical advection of vorticity at 2 and 6 km for Sally2. In these cases the two are nearly equal in the convective region, indicating that the contribution from Lagrangian tilting is relatively small.

There is some uncertainty to the conclusion that stretching dominates horizontal vorticity advection as there were no actual dropsondes contributing to the analysis in the neighborhood of the 2-km vortex during the critical period in which vortex alignment took place. However, the sudden development of anomalous winds of 15–20 m s^{-1} would be needed to advect 2-km vorticity from the old to the new location during the 3-h period of realignment, which were not detected by the observing platforms examined here. This is somewhat implausible, but not out of the question if the convection associated with the midlevel vortex strengthened enough to produce an impulsive low-level inflow while no soundings were available.

5. Discussion and conclusions

In this paper we use an unprecedented dataset (high altitude dropsondes from NOAA's G-IV, radar data from the G-IV and NOAA P-3 aircraft, ground radar, satellite images and satellite-detected lightning strikes) collected over 2 days (three G-IV flights) to analyze the RI of Hurricane Sally (2020) that occurred between the second (Sally2) and third (Sally3) G-IV flights. Shortly after the Sally2 observations, Sally underwent RI. The key question we wish to pose here is, can we predict the RI of Sally and, if so, what is the starting

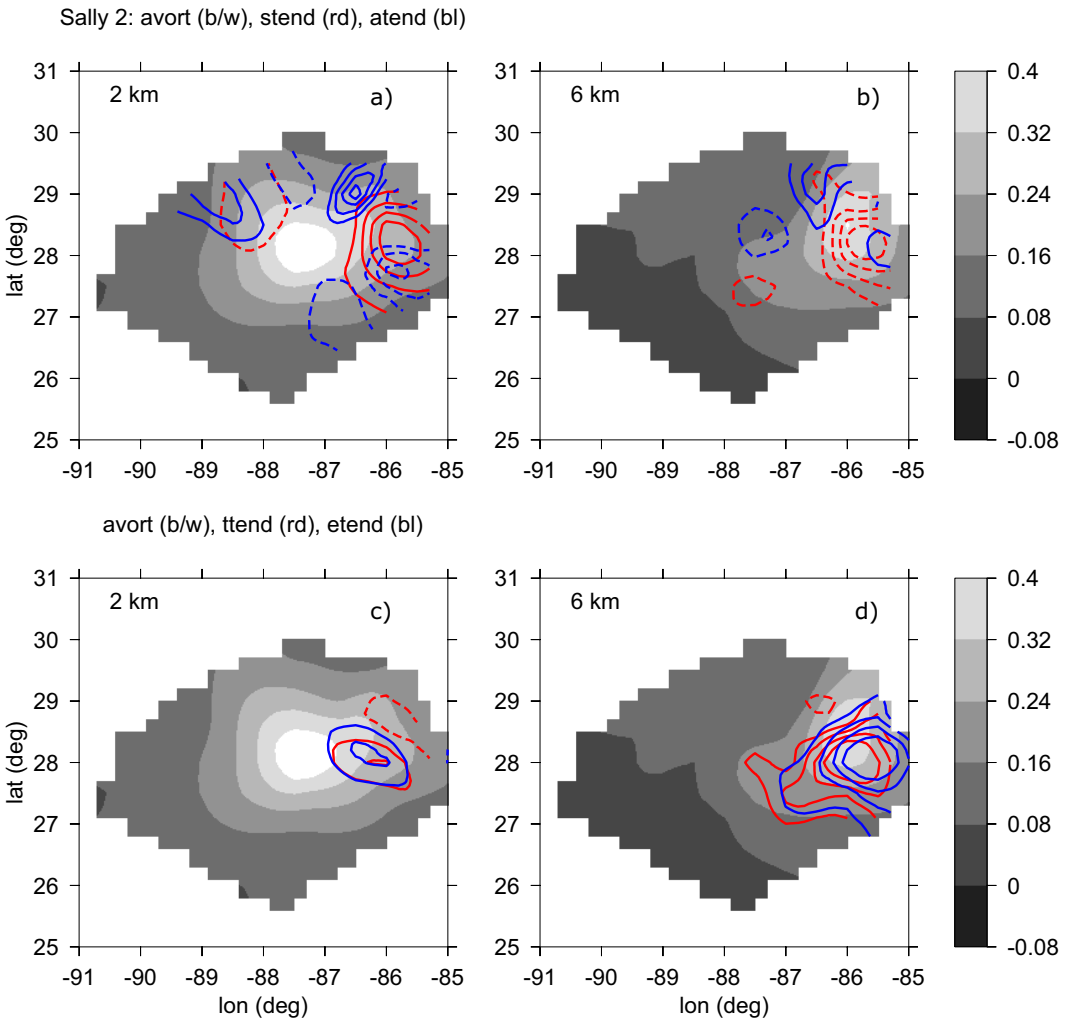

FIG. 15. Decomposition of the vorticity convergence tendency into advective and stretching components at (a) 2 and (b) 6 km. The absolute vorticity and vorticity tendencies are as indicated in Fig. 12, but the red contours show the stretching tendency (stend) and the blue contours show horizontal advective tendency (atend). (c),(d) The 2- and 6-km, respectively, Eulerian tilting (ttend; red) and the contribution to this from the vertical advection of vertical vorticity (etend; blue). As in Fig. 12, the contour interval for all tendencies is 0.006 ks^{-2} with solid and dashed contours indicating positive and negative values, respectively.

point after which we understand the subsequent chain of events? What are the key conditions of a storm that is about to experience RI?

Based on our analysis, one important condition supporting RI in Sally was the presence of a significant midlevel vortex. Such a vortex is associated with dynamically balanced thermal anomalies with warm anomalies above and cooler anomalies below, resulting in lower values of the instability index. Low instability index is associated with high saturation fraction; both of these variables are key indicators of strong, bottom-heavy upward mass flux as observations and modeling show. Sally2 satisfies these conditions. Low instability index and high saturation fraction are seen in Fig. 3, while bottom-heavy vertical mass flux profiles appear in Figs. 4 and 5. The midlevel vortex is evident in Figs. 4, 6, and 11.

Many developing TCs exhibit these conditions but most do not undergo RI. We therefore must look further, examining the pattern of vorticity tendencies in Sally. Sally2 in particular exhibited vorticity tendencies that bring the low and midlevel vortices into vertical alignment. Observations show that the 2-km vorticity tendency in Sally2 was sufficient to produce a strong 2-km vortex under the 6-km vortex in only 3 h via vorticity convergence. In addition, the tilting tendency at 6 km displaced the midlevel vortex slightly, thus aiding the alignment process. This evolution was unique to Sally2 and did not occur in Sally1. Figure 14 shows that the vortices at 2 and 6 km are indeed aligned in Sally3 only a few hours after they were misaligned in excess of 100 km.

Stepping back in the chain of causality, we need to address why a strong midlevel vortex existed in Sally2, but not a few

hours earlier in Sally1. The generation of a midlevel vortex by top-heavy convective mass flux profiles with strong midlevel convergence is the obvious mechanism to consider. However, the convection observed in both Sally1 and Sally2 was bottom-heavy with divergence occurring at 6 km. It is possible that top-heavy convection occurred between these two observational periods. Such convective bursts occurred episodically in Hermine (2016; Rogers et al. 2020) and were discussed in Bell and Montgomery (2019) for Hurricane Karl (2010). However, an alternative mechanism for the strengthening of the midlevel vortex is tilting. This conclusion is supported by the observation of a strong positive tilting tendency at 6 km in Sally2 that overcomes the negative stretching tendency near the preexisting vortex at this level in Fig. 13. Land-based radar indeed verified that strong convection existed in the 6-km vortex core during the critical period but could not distinguish between top-heavy and bottom-heavy cases. However, it developed, the midlevel vortex underwent considerable strengthening between Sally1 and Sally2.

The redevelopment of the 2-km vortex underneath the 6-km circulation in Sally2 was most likely affected primarily by vertical stretching produced by bottom-heavy mass flux profiles associated with the midlevel circulation. Horizontal advection of 2-km vorticity appeared to contribute minimally. An important, and fundamental, question to consider is whether the alignment of the 2- and 6-km circulations was a necessary precondition to intensification or whether the alignment occurred during an ongoing intensification period. In other words, does alignment cause intensification or is it simply one aspect of the structural evolution during intensification? It is true that Sally's intensity, according to the best track, was increasing prior to the observed alignment (cf. Figs. 1, 8, 10, 11), suggesting that alignment was not a cause of intensification. The best track is fairly coarse (6-h) temporal resolution, however, and there can be considerable uncertainty in intensity estimates, particularly for disorganized systems like Sally was prior to alignment. That being said, however, it is possible that Sally was intensifying at least some prior to the observed alignment after 1200 UTC 14 September. A close examination of the vorticity time–height series in Fig. 11a shows, though, that a significant increase in mid- to upper-level vorticity did not occur until 1–3 h after Sally's tilt decreased significantly. Additionally, although not shown here, Air Force reconnaissance missions on 14 September found Sally's central pressure did not begin to fall until 1200–1300 UTC, near the time when tilt was beginning to decrease (Fig. 11a). These observations indicate that alignment preceded the rapid improvement, and therefore RI, in Sally's structural organization. It seems reasonable to conclude that intensification can occur prior to alignment (provided there is deep convection in the vicinity of the MLC), but more substantial intensification, and perhaps rapid intensification, requires an alignment between the low- and midlevel circulation centers. Additional research is ongoing to explore this relationship further.

The pathway described here need not always be followed as there is more than one way to produce vortex alignment and RI (DesRosiers et al. 2022; Miyamoto and Nolan 2018). However, whatever the mechanism for RI, examination of vorticity tendencies associated with convective mass fluxes along with the thermodynamic processes responsible for this convection are likely to be productive, as this has the potential of distinguishing RI cases from less spectacular events. Further field projects with continuous high altitude dropsondes and research is needed to see how this is applicable to other reformation events as well as genesis (Zawislak et al. 2022).

Acknowledgments. This work was supported by the ONR Grant N000142012135, and NOAA base funds. We thank our reviewers for insightful and engaging comments.

Data availability statement. The P3 and G-IV TDR analyses used here can be readily downloaded at https://www.aoml.noaa.gov/ftp/pub/hrd/data/radar/level2/2020/sally/. The IR data used for the IR figures from the MERGIR database can be downloaded from https://disc.gsfc.nasa.gov/datasets/GPM_MERGIR_1/summary. 3D var analysis used here may be downloaded at https://github.com/stiposentic/sallyRI2022paper (Zenodo DOI: 10.5281/zenodo.6892773).

REFERENCES

Alvey, G. R., III, M. Fischer, P. Reasor, J. Zawislak, and R. Rogers, 2022: Observed processes underlying the favorable vortex repositioning early in the development of Hurricane Dorian (2019). *Mon. Wea. Rev.*, **150**, 193–213, https://doi.org/10.1175/MWR-D-21-0069.1.

Bell, M. M., and M. T. Montgomery, 2019: Mesoscale processes during the genesis of Hurricane Karl (2010). *J. Atmos. Sci.*, **76**, 2235–2255, https://doi.org/10.1175/JAS-D-18-0161.1.

——, M. Dixon, W.-C. Lee, B. Jarvornik, J. DeHart, and T.-Y. Cha, 2021: nsf-lrose/lrose-elle: Lrose-elle stable final release 20210312. Zenodo, accessed 1 February 2022, https://doi.org/10.5281/zenodo.5523312.

Berg, R., and B. J. Reinheart, 2021: National Hurricane Center tropical cyclone report: Hurricane Sally (11–17 September 2020). NHC Tech. Rep. AL192020, 69 pp., https://www.nhc.noaa.gov/data/tcr/AL192020_Sally.pdf.

Bretherton, C. S., M. E. Peters, and L. E. Back, 2004: Relationships between water vapor path and precipitation over the tropical oceans. *J. Climate*, **17**, 1517–1528, https://doi.org/10.1175/1520-0442(2004)017<1517:RBWVPA>2.0.CO;2.

Cangialosi, J. P., E. Blake, M. DeMaria, A. Penny, A. Latto, E. Rappaport, and V. Tallapragada, 2020: Recent progress in tropical cyclone intensity forecasting at the National Hurricane Center. *Wea. Forecasting*, **35**, 1913–1922, https://doi.org/10.1175/WAF-D-20-0059.1.

Chen, X., Y. Wang, J. Fang, and M. Xue, 2018: A numerical study on rapid intensification of Typhoon Vicente (2012) in the South China Sea. Part II: Roles of inner-core processes. *J. Atmos. Sci.*, **75**, 235–255, https://doi.org/10.1175/JAS-D-17-0129.1.

Corbosiero, K. L., and J. Molinari, 2002: The effects of vertical wind shear on the distribution of convection in tropical cyclones. *Mon. Wea. Rev.*, **130**, 2110–2123, https://doi.org/10.1175/1520-0493(2002)130<2110:TEOVWS>2.0.CO;2.

Daleu, C. L., and Coauthors, 2016: Intercomparison of methods of coupling between convection and large-scale circulation: 2.

Comparison over nonuniform surface conditions. *J. Adv. Model. Earth Syst.*, **8**, 387–405, https://doi.org/10.1002/2015MS000570.

DeMaria, M., M. Mainelli, L. K. Shay, J. A. Knaff, and J. Kaplan, 2005: Further improvements to the Statistical Hurricane Intensity Prediction Scheme (SHIPS). *Wea. Forecasting*, **20**, 531–543, https://doi.org/10.1175/WAF862.1.

DesRosiers, A. J., M. M. Bell, and T.-Y. Cha, 2022: Vertical vortex development in Hurricane Michael (2018) during rapid intensification. *Mon. Wea. Rev.*, **150**, 99–114, https://doi.org/10.1175/MWR-D-21-0098.1.

Emanuel, K. A., 1994: *Atmospheric Convection*. Oxford University Press, 580 pp.

Fischer, M. S., P. D. Reasor, R. F. Rogers, and J. F. Gamache, 2022: An analysis of tropical cyclone vortex and convective characteristics in relation to storm intensity using a novel airborne Doppler radar database. *Mon. Wea. Rev.*, **150**, 2255–2278, https://doi.org/10.1175/MWR-D-21-0223.1.

Fuchs-Stone, Ž.., D. J. Raymond, and S. Sentić, 2020: OTREC2019: Convection over the East Pacific and southwest Caribbean. *Geophys. Res. Lett.*, **47**, e2020GL087564, https://doi.org/10.1029/2020GL087564.

Gamache, J. F., 2005: Real-time dissemination of hurricane wind fields determined from airborne Doppler radar data. National Hurricane Center Tech. Rep., 38 pp., https://www.nhc.noaa.gov/jht/2003-2005reports/DOPLRgamache_JHTfinalreport.pdf.

Gao, J., M. Xue, A. Shapiro, and K. K. Droegemeier, 1999: A variational method for the analysis of three-dimensional wind fields from two Doppler radars. *Mon. Wea. Rev.*, **127**, 2128–2142, https://doi.org/10.1175/1520-0493(1999)127<2128:AVMFTA>2.0.CO;2.

Gjorgjievska, S., and D. J. Raymond, 2014: Interaction between dynamics and thermodynamics during tropical cyclogenesis. *Atmos. Chem. Phys.*, **14**, 3065–3082, https://doi.org/10.5194/acp-14-3065-2014.

Haynes, P. H., and M. E. McIntyre, 1987: On the evolution of vorticity and potential vorticity in the presence of diabatic heating and frictional or other forces. *J. Atmos. Sci.*, **44**, 828–841, https://doi.org/10.1175/1520-0469(1987)044<0828:OTEOVA>2.0.CO;2.

——, and ——, 1990: On the conservation and impermeability theorems for potential vorticity. *J. Atmos. Sci.*, **47**, 2021–2031, https://doi.org/10.1175/1520-0469(1990)047<2021:OTCAIT>2.0.CO;2.

Herman, M. J., and D. J. Raymond, 2014: WTG cloud modeling with spectral decomposition of heating. *J. Adv. Model. Earth Syst.*, **6**, 1121–1140, https://doi.org/10.1002/2014MS000359.

Hoskins, B. J., M. E. McIntyre, and A. W. Robertson, 1985: On the use and significance of isentropic potential vorticity maps. *Quart. J. Roy. Meteor. Soc.*, **111**, 877–946, https://doi.org/10.1002/qj.49711147002.

James, R. P., and P. M. Markowski, 2010: A numerical investigation of the effects of dry air aloft on deep convection. *Mon. Wea. Rev.*, **138**, 140–161, https://doi.org/10.1175/2009MWR3018.1.

Janowiak, J., B. Joyce, and P. Xie, 2017: NCEP/CPC L3 half hourly 4 km global (60S–60N) merged IR V1. Goddard Earth Sciences Data and Information Services Center (GES DISC), accessed 21 April 2022, https://doi.org/10.5067/P4HZB9N27EKU.

Juračić, A., and D. J. Raymond, 2016: The effects of moist entropy and moisture budgets on tropical cyclone development. *J. Geophys. Res. Atmos.*, **121**, 9458–9473, https://doi.org/10.1002/2016JD025065.

Kaplan, J., and M. DeMaria, 2003: Large-scale characteristics of rapidly intensifying tropical cyclones in the North Atlantic basin. *Wea. Forecasting*, **18**, 1093–1108, https://doi.org/10.1175/1520-0434(2003)018<1093:LCORIT>2.0.CO;2.

——, ——, and J. A. Knaff, 2010: A revised tropical cyclone rapid intensification index for the Atlantic and eastern North Pacific basins. *Wea. Forecasting*, **25**, 220–241, https://doi.org/10.1175/2009WAF2222280.1.

——, and Coauthors, 2015: Evaluating environmental impacts on tropical cyclone rapid intensification predictability utilizing statistical models. *Wea. Forecasting*, **30**, 1374–1396, https://doi.org/10.1175/WAF-D-15-0032.1.

Kilroy, G., M. T. Montgomery, and R. K. Smith, 2017a: The role of boundary-layer friction on tropical cyclogenesis and subsequent intensification. *Quart. J. Roy. Meteor. Soc.*, **143**, 2524–2536, https://doi.org/10.1002/qj.3104.

——, R. K. Smith, and M. T. Montgomery, 2017b: A unified view of tropical cyclogenesis and intensification. *Quart. J. Roy. Meteor. Soc.*, **143**, 450–462, https://doi.org/10.1002/qj.2934.

——, ——, and ——, 2018: The role of heating and cooling associated with ice processes on tropical cyclogenesis and intensification. *Quart. J. Roy. Meteor. Soc.*, **144**, 99–114, https://doi.org/10.1002/qj.3187.

López Carrillo, C., and D. J. Raymond, 2011: Retrieval of three-dimensional wind fields from Doppler radar data using an efficient two-step approach. *Atmos. Meas. Tech.*, **4**, 2717–2733, https://doi.org/10.5194/amt-4-2717-2011.

Maloney, E. D., and S. K. Esbensen, 2003: The amplification of east Pacific Madden–Julian oscillation convection and wind anomalies during June–November. *J. Climate*, **16**, 3482–3497, https://doi.org/10.1175/1520-0442(2003)016<3482:TAOEPM>2.0.CO;2.

——, and A. H. Sobel, 2004: Surface fluxes and ocean coupling in the tropical intraseasonal oscillation. *J. Climate*, **17**, 4368–4386, https://doi.org/10.1175/JCLI-3212.1.

Miyamoto, Y., and D. S. Nolan, 2018: Structural changes preceding rapid intensification in tropical cyclones as shown in a large ensemble of idealized simulations. *J. Atmos. Sci.*, **75**, 555–569, https://doi.org/10.1175/JAS-D-17-0177.1.

Molinari, J., and D. Vollaro, 2010: Distribution of helicity, CAPE, and shear in tropical cyclones. *J. Atmos. Sci.*, **67**, 274–284, https://doi.org/10.1175/2009JAS3090.1.

——, ——, and K. L. Corbosiero, 2004: Tropical cyclone formation in a sheared environment: A case study. *J. Atmos. Sci.*, **61**, 2493–2509, https://doi.org/10.1175/JAS3291.1.

——, P. Dodge, D. Vollaro, K. L. Corbosiero, and F. Marks Jr., 2006: Mesoscale aspects of the downshear reformation of a tropical cyclone. *J. Atmos. Sci.*, **63**, 341–354, https://doi.org/10.1175/JAS3591.1.

Neelin, J. D., O. Peters, and K. Hales, 2009: The transition to strong convection. *J. Atmos. Sci.*, **66**, 2367–2384, https://doi.org/10.1175/2009JAS2962.1.

Nguyen, L. T., and J. Molinari, 2015: Simulation of the downshear reformation of a tropical cyclone. *J. Atmos. Sci.*, **72**, 4529–4551, https://doi.org/10.1175/JAS-D-15-0036.1.

Raymond, D. J., 1992: Nonlinear balance and potential-vorticity thinking at large Rossby number. *Quart. J. Roy. Meteor. Soc.*, **118**, 987–1015, https://doi.org/10.1002/qj.49711850708.

——, 1995: Regulation of moist convection over the west Pacific warm pool. *J. Atmos. Sci.*, **52**, 3945–3959, https://doi.org/10.1175/1520-0469(1995)052<3945:ROMCOT>2.0.CO;2.

——, 2000: The Hadley circulation as a radiative–convective instability. *J. Atmos. Sci.*, **57**, 1286–1297, https://doi.org/10.1175/1520-0469(2000)057<1286:THCAAR>2.0.CO;2.

——, 2012: Balanced thermal structure of an intensifying tropical cyclone. *Tellus*, **64A**, 19181, http://doi.org/10.3402/tellusa.v64i0.19181.

——, and X. Zeng, 2005: Modelling tropical atmospheric convection in the context of the weak temperature gradient approximation. *Quart. J. Roy. Meteor. Soc.*, **131**, 1301–1320, https://doi.org/10.1256/qj.03.97.

——, and S. L. Sessions, 2007: Evolution of convection during tropical cyclogenesis. *Geophys. Res. Lett.*, **34**, L06811, https://doi.org/10.1029/2006GL028607.

——, and C. López Carrillo, 2011: The vorticity budget of developing Typhoon Nuri (2008). *Atmos. Chem. Phys.*, **11**, 147–163, https://doi.org/10.5194/acp-11-147-2011.

——, and M. M. Flores, 2016: Predicting convective rainfall over tropical oceans from environmental conditions. *J. Adv. Model. Earth Syst.*, **8**, 703–718, https://doi.org/10.1002/2015MS000595.

——, and G. Kilroy, 2019: Control of convection in high-resolution simulations of tropical cyclogenesis. *J. Adv. Model. Earth Syst.*, **11**, 1582–1599, https://doi.org/10.1029/2018MS001576.

——, and Ž. Fuchs-Stone, 2021a: Emergent properties of convection in OTREC and PREDICT. *J. Geophys. Res. Atmos.*, **126**, e2020JD033585, https://doi.org/10.1029/2020JD033585.

——, and ——, 2021b: Weak temperature gradient modeling of convection in OTREC. *J. Adv. Model. Earth Syst.*, **13**, e2021MS002557, https://doi.org/10.1029/2021MS002557.

——, G. B. Raga, C. S. Bretherton, J. Molinari, C. López-Carrillo, and Ž. Fuchs, 2003: Convective forcing in the intertropical convergence zone of the eastern Pacific. *J. Atmos. Sci.*, **60**, 2064–2082, https://doi.org/10.1175/1520-0469(2003)060<2064:CFITIC>2.0.CO;2.

——, C. S. Bretherton, and J. Molinari, 2006: Dynamics of the intertropical convergence zone of the east Pacific. *J. Atmos. Sci.*, **63**, 582–597, https://doi.org/10.1175/JAS3642.1.

——, S. L. Sessions, and Ž. Fuchs, 2007: A theory for the spinup of tropical depressions. *Quart. J. Roy. Meteor. Soc.*, **133**, 1743–1754, https://doi.org/10.1002/qj.125.

——, ——, A. H. Sobel, and Ž. Fuchs, 2009: The mechanics of gross moist stability. *J. Adv. Model. Earth Syst.*, **1**, 20, https://doi.org/10.3894/JAMES.2009.1.9.

——, ——, and C. López Carrillo, 2011: Thermodynamics of tropical cyclogenesis in the northwest Pacific. *J. Geophys. Res.*, **116**, D18101, https://doi.org/10.1029/2011JD015624.

——, S. Gjorgjievska, S. Sessions, and Ž. Fuchs, 2014: Tropical cyclogenesis and mid-level vorticity. *Aust. Meteor. Oceanogr. J.*, **64**, 11–25, https://doi.org/10.22499/2.6401.003.

——, Ž. Fuchs, S. Gjorgjievska, and S. Sessions, 2015: Balanced dynamics and convection in the tropical troposphere. *J. Adv. Model. Earth Syst.*, **7**, 1093–1116, https://doi.org/10.1002/2015MS000467.

Razin, M. N., and M. M. Bell, 2021: The unconventional eyewall replacement cycle of Hurricane Ophelia (2005). *Mon. Wea. Rev.*, **149**, 2151–2170, https://doi.org/10.1175/MWR-D-20-0181.1.

Reasor, P. D., R. Rogers, and S. Lorsolo, 2013: Environmental flow impacts on tropical cyclone structure diagnosed from airborne Doppler radar composites. *Mon. Wea. Rev.*, **141**, 2949–2969, https://doi.org/10.1175/MWR-D-12-00334.1.

Rios-Berrios, R., and R. D. Torn, 2017: Climatological analysis of tropical cyclone intensity changes under moderate vertical wind shear. *Mon. Wea. Rev.*, **145**, 1717–1738, https://doi.org/10.1175/MWR-D-16-0350.1.

——, C. A. Davis, and R. D. Torn, 2018: A hypothesis for the intensification of tropical cyclones under moderate vertical wind shear. *J. Atmos. Sci.*, **75**, 4149–4173, https://doi.org/10.1175/JAS-D-18-0070.1.

Rogers, R. F., and Coauthors, 2006: The Intensity Forecasting Experiment: A NOAA multiyear field program for improving tropical cyclone intensity forecasts. *Bull. Amer. Meteor. Soc.*, **87**, 1523–1538, https://doi.org/10.1175/BAMS-87-11-1523.

——, and Coauthors, 2013: NOAA's Hurricane Intensity Forecasting Experiment: A progress report. *Bull. Amer. Meteor. Soc.*, **94**, 859–882, https://doi.org/10.1175/BAMS-D-12-00089.1.

——, P. D. Reasor, J. A. Zawislak, and L. T. Nguyen, 2020: Precipitation processes and vortex alignment during the intensification of a weak tropical cyclone in moderate vertical shear. *Mon. Wea. Rev.*, **148**, 1899–1929, https://doi.org/10.1175/MWR-D-19-0315.1.

Schecter, D. A., and K. Menelaou, 2020: Development of a misaligned tropical cyclone. *J. Atmos. Sci.*, **77**, 79–111, https://doi.org/10.1175/JAS-D-19-0074.1.

Sentić, S., S. L. Sessions, and Ž. Fuchs, 2015: Diagnosing DYNAMO convection with weak temperature gradient simulations. *J. Adv. Model. Earth Syst.*, **7**, 1849–1871, https://doi.org/10.1002/2015MS000531.

Sessions, S. L., M. J. Herman, and S. Sentić, 2015: Convective response to changes in the thermodynamic environment in idealized weak temperature gradient simulations. *J. Adv. Model. Earth Syst.*, **7**, 712–738, https://doi.org/10.1002/2015MS000446.

Sherwood, S. C., 1999: Convective precursors and predictability in the tropical western Pacific. *Mon. Wea. Rev.*, **127**, 2977–2991, https://doi.org/10.1175/1520-0493(1999)127<2977:CPAPIT>2.0.CO;2.

Singh, M. S., and P. A. O'Gorman, 2013: Influence of entrainment on the thermal stratification in simulations of radiative-convective equilibrium. *Geophys. Res. Lett.*, **40**, 4398–4403, https://doi.org/10.1002/grl.50796.

Steiner, M., R. A. Houze Jr., and S. E. Yuter, 1995: Climatological characterization of three-dimensional storm structure from operational radar and rain gauge data. *J. Appl. Meteor. Climatol.*, **34**, 1978–2007, https://doi.org/10.1175/1520-0450(1995)034<1978:CCOTDS>2.0.CO;2.

Zawislak, J., and Coauthors, 2022: Accomplishments of NOAA's airborne hurricane field program and a broader future approach to forecast improvement. *Bull. Amer. Meteor. Soc.*, **103**, E311–E338, https://doi.org/10.1175/BAMS-D-20-0174.1.